

Computing spectral properties of topological insulators without artificial truncation or supercell approximation

Matthew J. Colbrook*, Andrew Horning†, Kyle Thicke‡, Alexander B. Watson§

Abstract

Topological insulators (TIs) are renowned for their remarkable electronic properties: quantised bulk Hall and edge conductivities, and robust edge wave-packet propagation, even in the presence of material defects and disorder. Computations of these physical properties generally rely on artificial periodicity (the supercell approximation), or unphysical boundary conditions (artificial truncation). In this work, we build on recently developed methods for computing spectral properties of infinite-dimensional operators. We apply these techniques to develop efficient and accurate computational tools for computing the physical properties of TIs. These tools completely avoid such artificial restrictions and allow one to probe the spectral properties of the infinite-dimensional operator directly, even in the presence of material defects and disorder. Our methods permit computation of spectra, approximate eigenstates, spectral measures, spectral projections, transport properties, and conductances. Numerical examples are given for the Haldane model, and the techniques can be extended similarly to other TIs in two and three dimensions.

Keywords: spectra, spectral measures, resolvent, topological insulators, edge states, conductivity

1 Introduction

Topological insulators (TIs) are materials with remarkable electronic properties¹. The bulk Hall and edge conductances of a TI are quantised precisely, even in the presence of defects and disorder (see [2, 6, 11, 13, 20, 21, 43, 53, 54, 61, 62, 66, 68, 81, 84, 85, 93] and the references therein). The remarkable robustness of these physical quantities has generated huge interest in TIs for potential industrial applications such as spintronics, quantum computing, and the “topological transistor” [11, 51, 61, 81, 85]. The importance of topological insulators was confirmed by the award of the 2016 Nobel prize to Thouless, Haldane, and Kosterlitz for foundational work on topological phases of matter.

The edge currents of TIs are mediated by electronic states localised at edges known as edge states. The robustness of the edge conductance of a TI can be seen at the level of localised wave-packets formed from these edge states, which snake around corners and defects of the edge, even in the presence of disorder [3, 11, 17, 19, 41, 46, 59, 61, 66, 75, 80, 81, 85, 93]. The behaviour of these wave-packets has spurred interest in building photonic and acoustic devices which mimic topological insulators for wave-guiding applications [38, 72, 86, 99, 100, 105].

The significant interest in TIs for industrial applications makes finding good numerical methods for computing their electronic properties essential. Non-interacting electrons in TIs are typically modelled by spatially discrete Schrödinger equations known as tight-binding models. In order to account for the vast number of ionic cores in typical materials, the bulk of the material is generally treated as

*Department of Applied Mathematics and Theoretical Physics, University of Cambridge and Centre Sciences des Données, Ecole Normale Supérieure, Paris.

Corresponding author: m.colbrook@damtp.cam.ac.uk

†Center for Applied Mathematics, Cornell University

‡Department of Mathematics, Technical University of Munich

§Mathematics Department, University of Minnesota Twin Cities, MN, USA.

¹For simplicity of presentation, in this work we treat topological insulators as synonymous with two-dimensional Chern insulators: two-dimensional topological insulators whose bulk topology is measured by the Chern number (the classification of topological insulators by dimension and symmetry class was given by [69, 91], for reviews, see [11, 47, 61, 81, 85]). Our methods are not fundamentally restricted to two dimensions or Chern insulators.

extending infinitely in all directions. In contrast, the edge of the material is modelled as a truncation of the infinite bulk model in one direction. The infinite extent of these models, coupled with non-periodic defects and disorder in realistic models, makes the numerical computation of the electronic properties of TIs very challenging.

In many scenarios, existing methods for computing electronic properties of TIs are unsatisfactory because they rely on imposing either artificial periodicity (supercell approximation), or unphysical boundary conditions (artificial truncations), or some combination of the two (see, for example, the package `PythTB` [104]). As far as we are aware, supercell approximation has not been rigorously justified in this context. In any case, it cannot be used in the direction transverse to an edge. At the same time, artificial truncation leads immediately to spectral pollution and spurious edge states [101].

This paper applies recently developed methods for rigorously and efficiently computing spectral properties of infinite-dimensional operators [23, 25–27, 31, 34, 35] to the problem of computing the electronic properties of TIs. We do this *without assuming model periodicity* and *without introducing artificial truncations*. From a numerical analysis perspective, the majority of methods that deal with spectra in infinite dimensions are of a “truncate-then-solve” flavour. A truncation/discretisation of the operator is adopted, possibly taking advantage of periodicity in suitable directions (e.g., supercell method), and methods for computing the eigenvalues of a finite matrix are used. In contrast, we adopt a “solve-then-discretise” approach. The “solve-then-discretise” paradigm has also recently been applied to other spectral problems [64, 101, 107], extensions of classical methods such as the QL and QR algorithms [30, 106], Krylov methods [52], and the computation of resonances [8, 9]. We are concerned with the following four types of spectral computations for infinite-dimensional operators:

- (P1) Computing **spectra** with error control and computing **approximate eigenstates**² discussed in Section 3.1, where we use the method of [35].
- (P2) Computing **spectral measures**, discussed in Section 3.2, where we use the method of [25, 34].
- (P3) Computing **spectral projections**, discussed in Section 3.3, for which we propose a new efficient method building on the ideas in [25, 34].
- (P4) Computing **transport properties** (and more generally the **functional calculus**), discussed in Section 3.4, where we use the method of [27].

With this set of computational tools in hand, we focus on computing the following physical properties of TIs:

- (PA) **Bulk** and **edge conductances** of non-periodic TIs, discussed in Sections 4.4 and 4.5, with results shown in Section 5.1.
- (PB) **Edge states** of periodic TIs and their **dispersion relations**, discussed in Section 4.5, with results shown in Section 5.2.
- (PC) **Approximate edge states** and **edge wave-packets** of non-periodic TIs, and their **spectral measures**, discussed in Section 4.5, with results shown in Sections 5.3 and 5.4.
- (PD) **Dynamics** of edge wave-packets of non-periodic TIs, discussed in Section 4.5, with results shown in Section 5.5.

For brevity, we have restricted ourselves to reporting results for the Haldane model [55]. However, our methods are not fundamentally restricted to this model and allow the computation of the electronic properties of more general TIs in two and three dimensions.

The paper is organised as follows. First, we discuss the motivation and idea of our methods in Section 2. We then give a summary of the algorithms in Section 3. The Haldane model and its physics are discussed in Section 4. Results are reported in Section 5. We also provide appendices of pseudocode, proofs and further details on the physical model.

Finally, code for our paper can be found at <https://github.com/SpecSolve/SpecTB> [33]. We hope this paper can also act as a user manual for those who wish to apply these techniques to their problems of interest.

²Where the spectrum is discrete, these approximate eigenstates are guaranteed to converge to exact eigenstates. This is sufficient to compute exact edge states of periodic TIs; see Section 4.5.

2 Motivation for the numerical methods

This work presents algorithms for discrete models commonly used to model electrons in materials known as tight-binding models. For such models, the Hilbert space is always isomorphic to the space of square summable sequences $l^2(\mathbb{N})$. Basis vectors correspond to atomic sites, perhaps with additional internal degrees of freedom such as sublattice label and spin. In this basis, the Hamiltonian is described by an infinite Hermitian matrix $\tilde{H} = \{\tilde{H}_{ij}\}_{i,j \in \mathbb{N}}$, which we assume to be sparse, or finite range, i.e. finitely many non-zero entries in each column.³ After a suitable ordering of the sites (e.g., by positional radius from an origin), there exists a function $f : \mathbb{N} \rightarrow \mathbb{N}$ such that $\tilde{H}_{ij} = 0$ if $i > f(j)$. Thus f describes the sparsity of \tilde{H} . We, therefore, describe the algorithms below for infinite sparse matrices representing Hermitian Hamiltonians. The restriction to sparse tight-binding models is not fundamental: for non-sparse matrices and even non-Hermitian operators, see [35]. Extensions of the algorithms to unbounded operators and partial differential operators can be found in the relevant papers [25, 27, 31, 34]. In this paper, **our aim is to compute the spectral quantities of interest from the infinite matrix \tilde{H} .**

2.1 Rectangular, as opposed to square, truncations

In the context of this paper, the algorithms we use rely on rectangular, as opposed to square, truncations of \tilde{H} . Since this may be an unfamiliar approach to the reader, we first explain the general idea before discussing the algorithms. See also [26] for a pedagogical description. In what follows, we use $\text{Sp}(\cdot)$ to denote the spectrum.

Model: As a concrete example, consider a finite range Hamiltonian on a hexagonal lattice such as the Haldane model. The situation is shown in Fig. 1 (panel (a)), where, for the sake of illustration, we have also added a physical edge (so that the model is a half lattice) as well as the position of a potential defect. The presence of the defect is significant because it breaks the translation symmetry of the system parallel to the edge, meaning that spectral properties cannot be computed (at least, not *exactly*, see the ‘supercell method’ below) using Bloch’s theorem⁴ parallel to the edge.

Previous approaches: Let P_n denote the orthogonal projection onto the linear span of the first n basis vectors. The most straightforward approach to computing spectral properties of the infinite operator H is to compute the spectral properties of large square truncations of the matrix \tilde{H} and hope that the computations converge in the limit of large truncations. Mathematically, this amounts to computing spectral properties of the finite-dimensional matrices $P_n \tilde{H} P_n$, where n is a large positive integer (shown as a red box in Fig. 1). Physically, this corresponds to studying the interactions of a finite number of sites within the truncation (Fig. 1 (b)). Although this method is straightforward, it is easy to see that the matrices $P_n \tilde{H} P_n$ can have eigenvalues that never approach the spectrum of H , even as $n \rightarrow \infty$. This is an example of the general phenomenon known as ‘spectral pollution’, where eigenvalues of finite discretisations/truncations can cluster in gaps between the essential spectrum of infinite self-adjoint operators [37, 73, 83] as the truncation size increases. In the context of TIs, which necessarily have eigenstates localised at edges, spectral pollution arising from the new edges created by the truncation is inevitable, see [101].

In the TI literature, a common approach (taken, e.g., in the package PythTB [104]) to computing spectral properties of H is the ‘supercell method on ribbon geometry’. The method involves two approximations. The first (the ‘supercell method’) is to approximate the edge of the material by a periodic edge with a large fundamental cell (the ‘supercell’) by repeating the defect along the edge. The spectral properties of the periodic edge are then related, via Bloch’s theorem, to those of the Hamiltonian restricted to a semi-infinite strip extending perpendicular to the edge with periodic (up to a phase) boundary conditions along the boundaries of the strip. The second approximation is then to truncate these semi-infinite Hamiltonians far from the original edge so that the computational domain forms a ‘ribbon’. Fig. 2 illustrates this approach.

³We use the notational $\tilde{\cdot}$ to distinguish between the abstract Hamiltonian H and its representation as an infinite matrix \tilde{H} on $l^2(\mathbb{N})$. This notation is to avoid confusion later on, where we write H in terms of infinite matrices acting on Hilbert spaces different to $l^2(\mathbb{N})$.

⁴Bloch’s theorem (see, for example, [1, 87]) states that eigenfunctions of periodic Hamiltonians can be decomposed as $\psi(\mathbf{r}) = e^{i\mathbf{k} \cdot \mathbf{r}} p(\mathbf{r})$ where p shares the periodicity of the Hamiltonian. Bloch’s theorem reduces spectral computations on infinite domains to computations (parametrised by \mathbf{k}) on domains that are bounded in each direction of periodicity, with periodic boundary conditions (up to a phase).

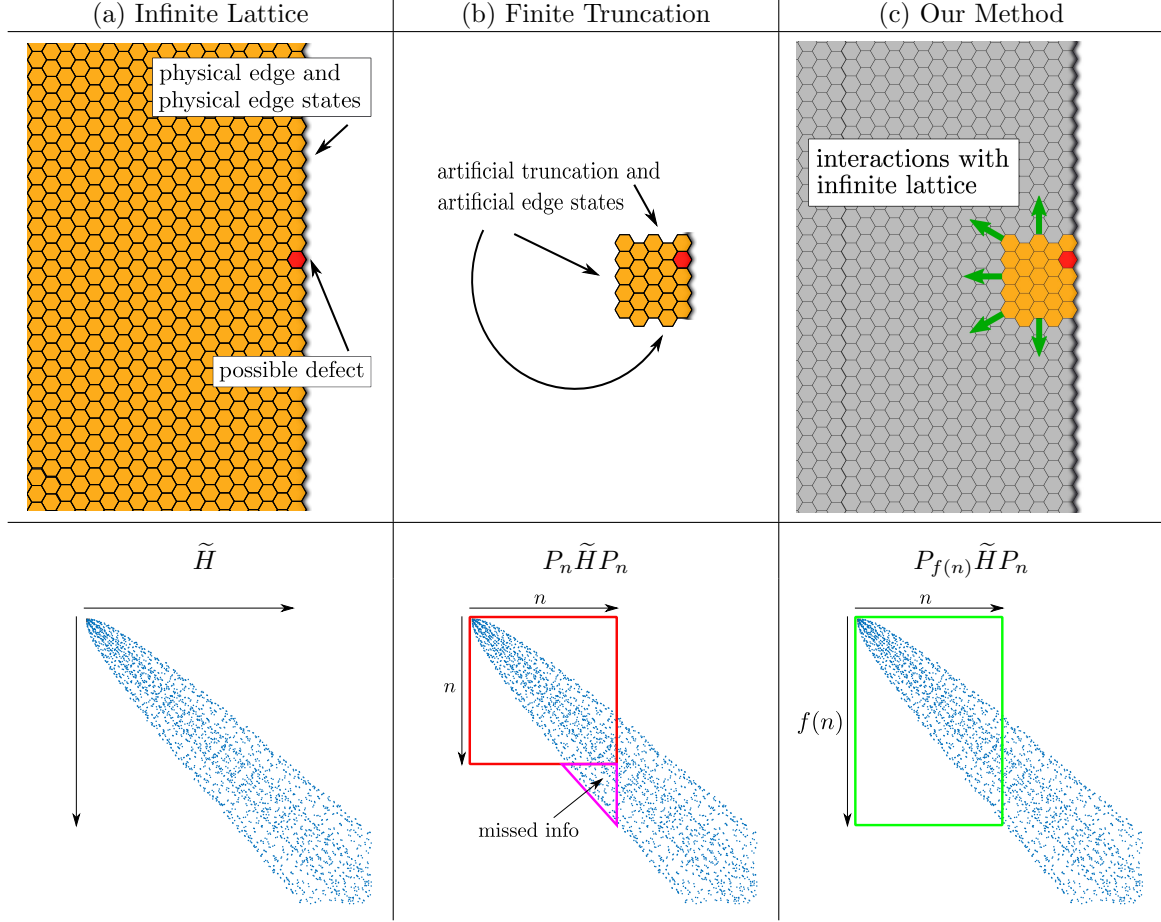


Figure 1: Top: (a) Infinite hexagonal lattice with an infinite edge and possible defect. (b) Finite truncation of tile to n sites. (c) Finite truncation with interactions shown as green arrows (our method). Bottom: The corresponding sparsity patterns (non-zero entries of the infinite matrix \tilde{H}). The boxes show the different types of truncations of the operator. In (c), $f(n)$ is chosen to include all of the interactions of the first n sites (basis vectors).

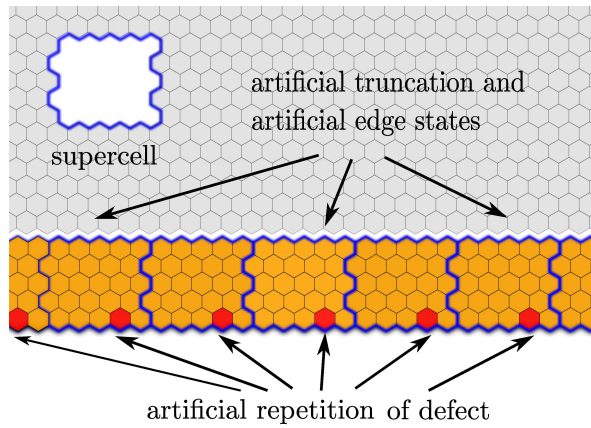


Figure 2: The supercell method on ribbon geometry combines periodic approximation along the edge with finite truncation away from the edge (note that the orientation of Fig. 1 has been rotated by $\pi/2$). The artificial edge typically leads to numerical artifacts in the computed spectrum. When the lattice contains defects or disorder, the artificial periodicity may also contribute to numerical artifacts or degrade accuracy.

Supercell approximations have been proved to converge as the supercell width increases in other contexts, see, e.g., [18, 42, 97], but we are not aware of any work justifying them in the present context. In practice, supercell approximations can be computationally inefficient when a large supercell is required, e.g., for materials with disorder (for a comprehensive discussion in the context of photonic quasicrystals, see [89]). As for the second approximation, spectral pollution is inevitable, leading to results that can be misleading and difficult to interpret (see Remark 1). It is worth remarking that the second approximation must be dealt with even when the supercell approximation is exact, e.g., when there is no defect at all! In certain circumstances, the second approximation can be removed (see Remark 2).

Remark 1. *It is common in the physics literature to accept the additional spectrum arising from the truncation away from the edge and simply treat the system as having a second edge. However, the spectrum of the truncated Hamiltonian is often clearly different from that of the semi-infinite operator: see, for example, Lee–Thorp [71], in particular Figure 26.7, and compare with Figure 5.3 of [101].*

Remark 2. *Two of the authors have introduced a method (the ‘Green’s function method’) which computes the discrete spectrum and associated eigenfunctions of the semi-infinite Hamiltonians obtained via supercell approximation which eliminates spectral pollution, see [101]. Similarly to the present work, the fundamental idea of the ‘Green’s function method’ is to work with the resolvent. The main contrast between [101] and the present work is that here we make fewer assumptions on the form of the edge Hamiltonian: we do not assume periodicity either parallel to the edge or into the bulk. We also compute other spectral properties not considered in [101]: spectral measure, spectral projection, and time propagation.*

Rectangular truncations: In this work, we compute spectral properties using rectangular truncations of the form (shown as a green box in Fig. 1):

$$P_{f(n)}\tilde{H}P_n \in \mathbb{C}^{f(n) \times n}. \quad (2.1)$$

Recall that f describes the sparsity pattern of the matrix. In our case, the rectangular truncation $P_{f(n)}\tilde{H}P_n$ corresponds to including all of the interactions of the first n sites (the first n columns of \tilde{H}) without needing to apply boundary conditions. Fig. 1 (panel (c)) shows the general idea. This truncation is in sharp contrast to naïve methods that typically take a square truncation of the matrix \tilde{H} , such as $P_n\tilde{H}P_n \in \mathbb{C}^{n \times n}$, with a boundary condition. This difference allows us to rigorously compute properties via computation of the resolvent operator

$$R(z, \tilde{H}) = (\tilde{H} - z)^{-1}, \quad z \notin \text{Sp}(H).$$

Once we have computed the resolvent, we can then compute the spectral properties of the operator H . This approach lends itself to adaptive computations of the full infinite-dimensional operator directly, eliminating *both* of the approximations involved in the ‘supercell method on ribbon geometry’. For our computational problems, this allows:

- (P1) Computation of spectra and approximate eigenstates with guaranteed error control. In the case of discrete spectrum, the approximate eigenstates correspond to bona fide eigenstates (e.g., edge states when the edge is periodic).
- (P2) & (P3) Computation of spectral measures/projections with guaranteed convergence and given rates of approximation.
- (P4) Computation of the functional calculus (and hence transport properties) with guaranteed error control.

With this technique in hand, we can reliably probe the spectral properties of systems in infinite dimensions. Indeed, this technique is already allowing for the discovery and investigation of new physics in quasicrystalline systems, including their transport and topological properties [65].

Remark 3 (Foundations of computation). *Our methods form part of a wider programme on the foundations of computations. One can classify computational spectral problems (and other types of computational problems) into a hierarchy (the SCI hierarchy) [7, 10, 22–25, 30, 31, 60, 90]. This measures*

the intrinsic difficulty of computational problems and provides proofs of the optimality of algorithms, realising the limits of what computers can achieve. Beyond spectral theory, this framework is now being applied to optimisation, machine learning and artificial intelligence, solving partial differential equations, and computer-assisted proofs⁵ [4, 5, 8, 9, 27, 28, 107]. The SCI hierarchy generalises S. Smale's seminal work [95, 96] with L. Blum, F. Cucker, M. Shub [15, 16] and his program on the foundations of scientific computing and existence of algorithms pioneered by C. McMullen [78, 79] and P. Doyle & C. McMullen [40]. As science and society become increasingly reliant on computations, it is essential to understand what is computationally possible and design algorithms that are optimal and achieve these bounds. For the sake of brevity, we have omitted this wider framework, but invite the interested reader to consult the above references.

3 The infinite-dimensional numerical methods

Here we briefly describe the algorithms for infinite-dimensional spectral computations. Pseudocode is provided in Appendix A.

3.1 Computation of spectra and approximate eigenstates

We utilise an algorithm, developed in [35], that computes the spectrum of an infinite-dimensional operator with error control. Recall that in our setting, the Hamiltonian H can be represented by an infinite Hermitian matrix, $\tilde{H} = \{\tilde{H}_{ij}\}_{i,j \in \mathbb{N}}$ and we are given a function $f : \mathbb{N} \rightarrow \mathbb{N}$ such that $\tilde{H}_{ij} = 0$ if $i > f(j)$. Thus f describes the sparsity of \tilde{H} . Our starting point is the function

$$F_n(z) := \sigma_{\inf}(P_{f(n)}(\tilde{H} - z)P_n), \quad (3.1)$$

where we remind the reader that P_m denotes the orthogonal projection onto the linear span of the first m basis vectors. We also use σ_{\inf} to denote the smallest singular value of the corresponding rectangular matrix. Since our operator is normal (commutes with its adjoint), the function F is an upper bound for the distance of z to the spectrum $\text{Sp}(H)$, and converges down to this distance uniformly on compact sets as $n \rightarrow \infty$ [35]. Physically, $F_n(z)$ is the square-root of the ground state energy of the folded Hamiltonian $P_n(\tilde{H} - z)^*(\tilde{H} - z)P_n$. There are numerous ways to compute F_n , such as standard iterative algorithms or incomplete Cholesky decomposition of the shifts $P_n(\tilde{H} - z)^*P_{f(n)}(\tilde{H} - z)P_n$ (see the supplementary material of [35] for a discussion). The other ingredient we need is a grid of points $G_n = \{z_1^{(n)}, \dots, z_{j(n)}^{(n)}\} \subset \mathbb{R}$ providing the wanted resolution r_n over the spectral region of interest.

The method is sketched in Algorithm 1 and produces three quantities: Γ_n , E_n and V_n . The simple idea of the method is a local search routine. If $F_n(z) \leq 1/2$, we search within a radius $F_n(z)$ around z to minimise the approximated distance to the spectrum. This gives our best estimate of points in the spectrum near z (the set M_z). The output $\Gamma_n(H)$ is then the collection of these local minimisers. $\Gamma_n(H)$ converges to the spectrum $\text{Sp}(H)$ of the full infinite-dimensional operator as $n \rightarrow \infty$ (for suitable $r_n \rightarrow \infty$). This convergence is free from the edge states/spectral pollution that are associated with any artificial or numerical truncation. In other words, we compute $\text{Sp}(H)$, and only $\text{Sp}(H)$. Note that in the examples of this paper, $\text{Sp}(H)$ does include spectrum associated to edge states of the full Hamiltonian H . The algorithm also outputs an error bound E_n that satisfies

$$\sup_{z \in \Gamma_n(H)} \text{dist}(z, \text{Sp}(H)) \leq E_n \quad \text{with} \quad \lim_{n \rightarrow \infty} E_n = 0. \quad (3.2)$$

For an accuracy $\delta > 0$, we simply increase n until $E_n \leq \delta$. The final quantity V_n consists of the approximate states corresponding to the output Γ_n . The approximate eigenstate $v_n(z)$ satisfies

$$\|(\tilde{H} - z)v_n(z)\| = \|P_{f(n)}(\tilde{H} - z)P_nv_n(z)\| = F_n(z) \leq E_n,$$

up to numerical errors. For an interval arithmetic implementation of this algorithm (allowing verified error bounds) and extensions to partial differential operators, see [31]. We can also verify the spectral content of these approximate eigenstates by computing their spectral measure, see Section 3.2.

⁵See for example the work by C. Fefferman & L. Seco (Dirac-Schwinger conjecture) [44, 45] and T. Hales et. al (Kepler's conjecture/Hilbert's 18th problem) [57, 58] that implicitly prove results in the SCI hierarchy.

3.2 Computation of scalar spectral measures

Associated with the Hamiltonian H is a projection-valued measure, \mathcal{E} , whose existence is guaranteed by the spectral theorem [88, Theorem VIII.6] and whose support is the spectrum $\text{Sp}(H)$. This diagonalises H , even when there does not exist a basis of normalisable eigenstates (recall that we are working in an infinite-dimensional Hilbert space):

$$H = \int_{\text{Sp}(H)} \lambda \, d\mathcal{E}(\lambda). \quad (3.3)$$

In finite dimensions, or when H is compact or has compact resolvent, \mathcal{E} consists of a sum of Dirac measures, located at the eigenvalues of H , whose values are the corresponding projections onto eigenspaces. More generally, however, there may be a continuous component of the spectrum and spectral measure.

The key ingredient that allows approximations of \mathcal{E} to be computed is the formula for the resolvent

$$(H - z)^{-1} = \int_{\text{Sp}(H)} \frac{1}{\lambda - z} \, d\mathcal{E}(\lambda). \quad (3.4)$$

In [25], it is shown how to compute the action of the resolvent with error control via the rectangular truncations $P_{f(n)}(\tilde{H} - z)P_n$ and solving the resulting overdetermined linear system in the least squares sense. The residual converges to zero as $n \rightarrow \infty$ and can be used to provide the needed error bounds through an adaptive selection of n [25, Theorem 2.1]. Using this, we compute a smoothed approximation of \mathcal{E} via convolution with a rational kernel K_ϵ for smoothing parameter $\epsilon > 0$.

We explain the method for the important case of scalar-valued measures, before discussing the case of spectral projections in Section 3.3. The spectral measure of H with respect to $\psi \in \mathcal{H}$ is a scalar measure defined as $\mu_\psi(\Omega) := \langle \mathcal{E}(\Omega)\psi, \psi \rangle$. Lebesgue's decomposition of μ_ψ [98] gives

$$d\mu_\psi(y) = \underbrace{\sum_{\lambda \in \text{Sp}_p(H)} \langle \mathcal{P}_\lambda \psi, \psi \rangle \delta(y - \lambda) dy}_{\text{discrete part}} + \underbrace{\rho_\psi(y) dy + d\mu_\psi^{(\text{sc})}(y)}_{\text{continuous part}}. \quad (3.5)$$

The discrete part of μ_ψ is a sum of Dirac delta distributions on the set of eigenvalues of H , which we denote by $\text{Sp}_p(H)$. The coefficient of each δ in the sum is $\langle \mathcal{P}_\lambda \psi, \psi \rangle = \|\mathcal{P}_\lambda \psi\|^2$, where \mathcal{P}_λ is the orthogonal spectral projector associated with the eigenvalue λ . The continuous part of μ_ψ consists of an absolutely continuous part with Radon–Nikodym derivative $\rho_\psi \in L^1(\mathbb{R})$ and a singular continuous component $\mu_\psi^{(\text{sc})}$.

We evaluate smoothed approximations of μ_ψ via a function g_ϵ , with smoothing parameter $\epsilon > 0$, that converges weakly to μ_ψ [14, Ch. 1]. That is,

$$\int_{\mathbb{R}} \phi(y) g_\epsilon(y) \, dy \rightarrow \int_{\mathbb{R}} \phi(y) \, d\mu_\psi(y), \quad \text{as } \epsilon \downarrow 0,$$

for any bounded, continuous function ϕ . The classical example of this is Stone's formula which corresponds to convolution with the Poisson kernel

$$g_\epsilon(x) = \frac{1}{2\pi i} \langle [(H - (x + i\epsilon))^{-1} - (H - (x - i\epsilon))^{-1}] \psi, \psi \rangle = \int_{\mathbb{R}} \frac{\epsilon \pi^{-1}}{(x - \lambda)^2 + \epsilon^2} \, d\mu_\psi(\lambda). \quad (3.6)$$

As $\epsilon \downarrow 0$, this approximation converges weakly to μ_ψ . However, for a given truncation size, if ϵ is too small the approximation of (3.6) via $P_{f(n)}(\tilde{H} - z)P_n$ (described above) becomes unstable due to the truncation of \tilde{H} . There is an increased computational cost for smaller ϵ , which typically requires larger truncation parameters. Since we want to approximate spectral properties without finite-size effects, it is advantageous to replace the Poisson kernel with higher-order rational kernels developed in [34]. These kernels have better convergence rates as $\epsilon \downarrow 0$, allowing a larger ϵ to be used for a given accuracy, thus leading to a lower computational burden. We use the high-order kernel machinery developed in [34], where the following definition is made.

Definition 3.1 (*m*th order kernel). *Let $m \in \mathbb{N}$ and $K \in L^1(\mathbb{R})$. We say K is an m th order kernel if:*

- (i) *Normalised: $\int_{\mathbb{R}} K(x) \, dx = 1$.*

(ii) *Zero moments:* $K(x)x^j$ is integrable and $\int_{\mathbb{R}} K(x)x^j dx = 0$ for $0 < j < m$.

(iii) *Decay at $\pm\infty$:* There is a constant C_K , such that $|K(x)| \leq C_K(1 + |x|)^{-(m+1)}$, $\forall x \in \mathbb{R}$.

We set $K_\epsilon(\cdot) = \epsilon^{-1}K(\cdot/\epsilon)$ to obtain an approximate identity. High-order kernels can be constructed using rational functions as follows. Let $\{a_j\}_{j=1}^m$ be distinct points in the upper half plane and suppose that the constants $\{\alpha_j\}_{j=1}^m$ satisfy the following (transposed) Vandermonde system:

$$\begin{pmatrix} 1 & \dots & 1 \\ a_1 & \dots & a_m \\ \vdots & \ddots & \vdots \\ a_1^{m-1} & \dots & a_m^{m-1} \end{pmatrix} \begin{pmatrix} \alpha_1 \\ \alpha_2 \\ \vdots \\ \alpha_m \end{pmatrix} = \begin{pmatrix} 1 \\ 0 \\ \vdots \\ 0 \end{pmatrix}. \quad (3.7)$$

Then the kernel

$$K(x) = \frac{1}{2\pi i} \sum_{j=1}^m \frac{\alpha_j}{x - a_j} - \frac{1}{2\pi i} \sum_{j=1}^m \frac{\bar{\alpha}_j}{x - \bar{a}_j}, \quad (3.8)$$

is an m th order kernel, and we have the following generalisation of Stone's formula

$$\begin{aligned} [K_\epsilon * \mu_\psi](x) &= \frac{-1}{2\pi i} \sum_{j=1}^m \langle [\alpha_j(H - (x - \epsilon a_j))^{-1} - \bar{\alpha}_j(H - (x - \epsilon \bar{a}_j))^{-1}] \psi, \psi \rangle \\ &= \frac{-1}{\pi} \sum_{j=1}^m \text{Im}(\alpha_j \langle (H - (x - \epsilon a_j))^{-1} \psi, \psi \rangle). \end{aligned} \quad (3.9)$$

This convolution converges with m th order of convergence in ϵ (up to a logarithmic factor and for sufficiently smooth μ_ψ) [34]. The second line of (3.9) follows from the conjugate symmetry of the resolvent. Here, \bar{z} denotes the complex conjugate of z and $*$ represents convolution. As a natural extension of the Poisson kernel, whose two poles are at $\pm i$, we consider the choice $a_j = 2j/(m+1) - 1 + i$. We then determine the residues by solving the Vandermonde system in (3.7). The first six kernels are explicitly written down in Table 1 (taken from [34]).

Given an m th order rational kernel, defined by distinct poles a_1, \dots, a_m in the upper half-plane, the resolvent-based framework for evaluating an approximation of the spectral measure μ_ψ is summarised in Algorithm 2. This algorithm, which can be performed in parallel for several x_0 , forms the foundation of **SpecSolve** [32]. In practice, the resolvent in Algorithm 2 is discretised before being applied. We compute an accurate value of μ_ψ^ϵ provided that the resolvent is applied with sufficient accuracy, which can be done *adaptively* with *a posteriori* error bounds [25]. For an efficient adaptive implementation, **SpecSolve** constructs a fixed discretisation, solves linear systems at each required complex shift, and checks the approximation error at each shift. If further accuracy is needed at a subset of the shifts, then the discretisation is refined geometrically, applied at these shifts, and the error is recomputed. This process is repeated until the resolvent is computed accurately at all shifts.

3.3 Computation of spectral projections

Given an interval $[a, b] \subset \text{Sp}(H)$, a vector $\psi \in \mathcal{H}$, and an m th order kernel K , the identity

$$[K_\epsilon * \mathcal{E}](x) = \frac{-1}{2\pi i} \sum_{j=1}^m [\alpha_j(H - (x - \epsilon a_j))^{-1} - \bar{\alpha}_j(H - (x - \epsilon \bar{a}_j))^{-1}] \quad (3.10)$$

allows us to approximate $\mathcal{E}([a, b])\psi$ by solving shifted linear system of the form $(H - z)u = \psi$. Employing a quadrature rule with weights w_1, \dots, w_ℓ and nodes x_1, \dots, x_ℓ , we form the approximation

$$\int_a^b [K_\epsilon * \mathcal{E}](x) dx \approx \frac{-1}{2\pi i} \sum_{\ell=1}^N w_\ell \sum_{j=1}^m [\alpha_j(H - (x_\ell - \epsilon a_j))^{-1} - \bar{\alpha}_j(H - (x_\ell - \epsilon \bar{a}_j))^{-1}]. \quad (3.11)$$

The following generalisation of Stone's formula establishes that the approximation converges in the limit $\epsilon \rightarrow 0$, up to contributions from atoms of \mathcal{E} at the endpoints. It is convenient to distinguish between the real and imaginary parts of the residues explicitly, so we denote $\alpha_j = \beta_j + i\gamma_j$.

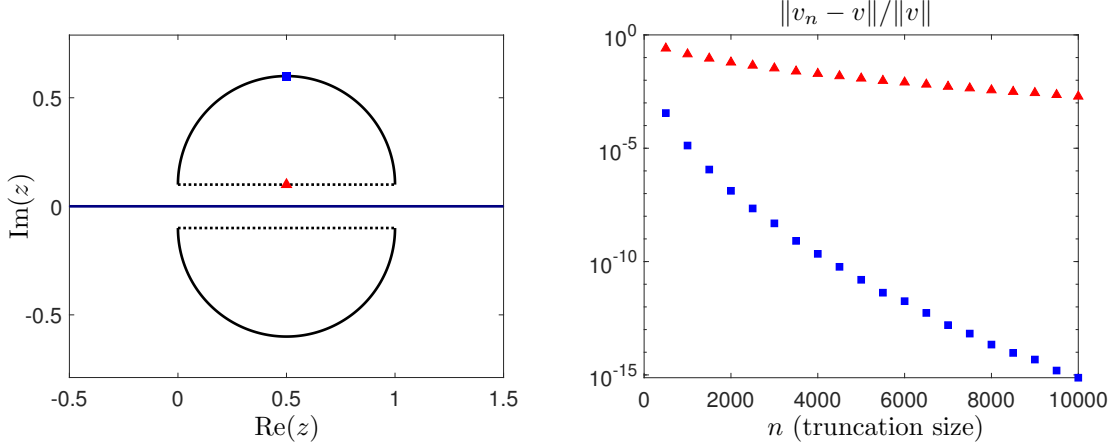


Figure 3: Deforming the contour of integration away from the spectrum of H in (3.11) alleviates the computational cost of computing the resolvent at the interior quadrature nodes. The left panel depicts two integration contours (solid and dashed lines) for the Poisson kernel ($m = 1$) with smoothing parameter $\epsilon = 0.1$. The right panel displays the relative approximation errors in the solutions of the truncated system $(P_{f(n)}\tilde{H}P_n - z)v_n = e_1$ (see Section 2.1), where e_1 is the first canonical basis vector and \tilde{H} is the Hamiltonian of the bulk Haldane model (see Section 4.1), corresponding to the two values of z marked along the contours in the left panel (blue square and red triangle).

Theorem 3.2. *Given a projection-valued measure \mathcal{E} (see (3.3)) and m th order kernel K with conjugate pole pairs (see (3.8)), for any $[a, b] \subset \mathbb{R}$ we have that*

$$\lim_{\epsilon \rightarrow 0^+} \int_a^b [K_\epsilon * \mathcal{E}](x) dx = \mathcal{E}((a, b)) + c_l \mathcal{E}(\{a\}) + c_r \mathcal{E}(\{b\}),$$

where $c_l = \pi^{-1} \sum_{j=1}^m \beta_j (\pi - \arg(a_j)) + i\gamma_j \log |a_j|$ and $c_r = \pi^{-1} \sum_{j=1}^m \beta_j \arg(a_j) - i\gamma_j \log |a_j|$. Moreover, if the poles are symmetric about the imaginary axis so that $a_{m+1-j} = -\bar{a}_j$, then $c_l = c_r = 1/2$.

Proof. See Appendix B. □

Remark 4 (Contribution of singleton sets). *One can easily show via the dominated convergence theorem that*

$$\lim_{\epsilon \rightarrow 0^+} \frac{\epsilon}{2i} [(H - x - i\epsilon)^{-1} - (H - x + i\epsilon)^{-1}] = \mathcal{E}(\{x\}).$$

Together with Theorem 3.2, this allows computation of $\mathcal{E}((a, b))$ and $\mathcal{E}([a, b])$.

By analogy with scalar spectral measures, approximating projection-valued spectral measures with higher-order rational convolution kernels is computationally advantageous because they achieve comparable accuracy with larger ϵ . By increasing the kernel order rather than decreasing ϵ , the resolvent in (3.11) remains well-conditioned and is usually significantly cheaper to apply. In addition, we can reduce the computational cost further by leveraging the resolvent's analyticity in the upper and lower half-plane and deforming the contour of integration in (3.11) away from the spectrum (see Fig. 3 (left)).

Consider the semi-circle contour connecting the points a and b and oriented in the clockwise direction, parametrised explicitly by $0 \leq \theta \leq 1$ as

$$z(\theta) = b + \frac{a-b}{2}(1 + \exp(i\pi\theta)), \quad \text{with} \quad z'(\theta) = i\pi \frac{a-b}{2} \exp(i\pi\theta).$$

Since the resolvent is analytic in $\mathbb{C} \setminus \text{Sp}(H)$ and a_1, \dots, a_m lie in the upper half-plane, we may write

$$\begin{aligned} \int_a^b [K_\epsilon * \mathcal{E}](x) dx &= \frac{-1}{2\pi i} \int_0^1 \sum_{j=1}^m [\alpha_j (H - (z(\theta) - \epsilon a_j))^{-1} z'(\theta) - \bar{\alpha}_j (H - (\bar{z}(\theta) - \epsilon \bar{a}_j))^{-1} \bar{z}'(\theta)] dz \\ &\approx \frac{-1}{2\pi i} \sum_{\ell=1}^N \tilde{w}_\ell \sum_{j=1}^m [\alpha_j (H - (z(\theta_\ell) - \epsilon a_j))^{-1} z'(\theta_\ell) - \bar{\alpha}_j (H - (\bar{z}(\theta_\ell) - \epsilon \bar{a}_j))^{-1} \bar{z}'(\theta_\ell)]. \end{aligned} \quad (3.12)$$

with quadrature weights $\tilde{w}_1, \dots, \tilde{w}_N$ and nodes $\theta_1, \dots, \theta_N$. From a computational standpoint, (3.12) improves two-fold on the formulation in (3.11):

- First, the resolvent is evaluated further from the spectrum and is typically well-approximated by smaller discretisations at many interior quadrature nodes (see Fig. 3 (right)).
- Second, the convergence rate of quadrature rules are improved because the integrand's region of analyticity is effectively enlarged when the contour is deformed away from the spectrum (see Fig. 4) [56]. Consequently, fewer quadrature nodes are required to approximate the integral to a fixed tolerance.

Therefore, comparable accuracy is achieved while solving both fewer and smaller linear systems.

To compare the computational efficiency of the two contours with respect to the second point, we estimate the number of quadrature nodes required to achieve approximation error $0 < \delta_* < 1$. We consider spectral projection onto the interval $[0, 1]$ (without loss of generality), Clenshaw–Curtis quadrature (CCQ), and an m th order rational kernel with equispaced poles $a_j = 2j/(m+1) - 1 + i$ (see Section 3.2). In this setting, Clenshaw–Curtis converges exponentially so that the quadrature approximation error is bounded by $\|E_N\| \leq C\rho^{-N}$, where N is the number of quadrature nodes, $\rho > 1$ is half the sum of the major and minor axes of any Bernstein ellipse B_ρ with foci at 0 and 1 in which $[K_\epsilon * \mathcal{E}](x)$ is analytic, and $C > 0$ is a constant proportional to $\sup_{z \in B_\rho} \|[K_\epsilon * \mathcal{E}](z)\|$. The minimal number of nodes required to achieve $\|E_N\| \leq \delta_*$ error is therefore $N \approx \log(C/\delta_*) / \log \rho$.

To estimate the convergence rate ρ for each contour, suppose the singularities of $[K_\epsilon * \mathcal{E}](x)$ are determined precisely by the spectrum of H .⁶ For the flat contour (see (3.11)), the integrand is analytic between parallel lines displaced from the contour of integration by $\pm i\epsilon$ in the complex x -plane (see Fig. 4, left). We consider the elliptic region of analyticity with minor axis $(\rho_1 - \rho_1^{-1})/2 = \epsilon$, so that

$$\rho_1 = \epsilon + \sqrt{\epsilon^2 + 1} = 1 + \mathcal{O}(\epsilon) \quad \text{as} \quad \epsilon \rightarrow 0.$$

For the deformed contour (see (3.12)), the integrand's region of analyticity is bounded by the curves in the complex θ -plane defined by $z(\theta) - \epsilon a_j \in \text{Sp}(H)$ for $j = 1, \dots, m$ (see Fig. 4, right). Here, we may take the Bernstein ellipse with major axis $(\rho_2 + \rho_2^{-1})/2 = 1 + \epsilon/2$, so that

$$\rho_2 = 1 + \epsilon/2 + \sqrt{(1 + \epsilon/2)^2 - 1} = 1 + \mathcal{O}(\sqrt{\epsilon}), \quad \text{as} \quad \epsilon \rightarrow 0.$$

Since H is self-adjoint, $\sup_{z \in B_\rho} \|[K_\epsilon * \mathcal{E}](z)\|$ grows in inverse proportion to $\text{dist}(B_\rho, \text{Sp}(H))$ as does the constant C . For both contours, our choice of B_ρ yields $C = \mathcal{O}(\epsilon^{-1})$. Therefore, we conclude that the number of quadrature nodes required on each contour is, as $\epsilon \rightarrow 0$,

$$N_1 \approx \frac{\log(C/\delta_*)}{\log \rho_1} = \mathcal{O}(\epsilon^{-1} \log(\epsilon^{-1} \delta_*^{-1})), \quad \text{and} \quad N_2 \approx \frac{\log(C/\delta_*)}{\log \rho_2} = \mathcal{O}\left(\epsilon^{-\frac{1}{2}} \log(\epsilon^{-1} \delta_*^{-1})\right).$$

The deformed contour improves on (3.11) by requiring a factor of up to $\mathcal{O}(\sqrt{\epsilon})$ fewer CCQ nodes. This analysis also reveals the further benefit of a reduced number of quadrature nodes when increasing ϵ using high-order kernels.⁷

3.4 Computing transport properties and the functional calculus

For the computation of general semigroups with error control using rectangular truncations, we refer the reader to [27, 29]. Related to the method we adopt here, many works use contour methods to invert the Laplace transform and solve time evolution problems, with a focus on parabolic PDEs [39, 48, 49, 74, 77, 94, 108, 109]. An excellent survey of contour methods is provided in [103].

In our case, the relevant Hamiltonians are bounded and the procedure is considerably simplified. For a holomorphic function g , Cauchy's integral formula yields

$$g(H) = \frac{1}{2\pi i} \int_\gamma g(z)(H - z)^{-1} dz, \quad (3.13)$$

⁶In fact, $[K_\epsilon * \mathcal{E}](x)$ may sometimes be analytically continued across the spectrum of H , in which case CCQ may converge faster than our analysis indicates for both contours.

⁷Under certain smoothness conditions we can take $\epsilon = \mathcal{O}(\delta_*^{1/m})$ up to logarithmic factors.

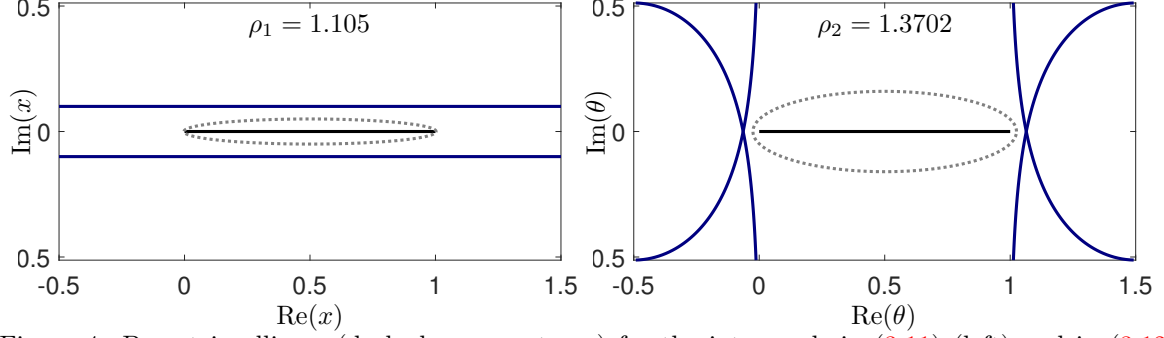


Figure 4: Bernstein ellipses (dashed grey contours) for the integrands in (3.11) (left) and in (3.12) (right) with $m = 1$ and $\epsilon = 0.1$. The integrand in (3.12) is analytic in a larger ellipse because the spectrum of H is effectively deformed away (blue lines) from the integration contour (black line). The ellipse parameters ρ_1 and ρ_2 govern convergence rates for the Clenshaw–Curtis quadrature approximations in (3.11) and (3.12), respectively.

where γ is a closed contour looping once around the spectrum. Transport properties are computed via the choice $g(z) = \exp(-izt)$. Namely, given an initial wavefunction ψ_0 , we wish to compute

$$\psi(t) = \exp(-iHt)\psi_0 = \frac{1}{2\pi i} \int_{\gamma} \exp(-izt) [(H - z)^{-1}\psi_0] dz. \quad (3.14)$$

The contour integral is computed using quadrature and approximations of the resolvent $(H - z)^{-1}$ via rectangular truncations as above. In particular, the rectangular truncation of the Hamiltonian is chosen adaptively through *a posteriori* error bounds. This allows us to perform rigorous computations with error control that are guaranteed to be free from finite-size or truncation/discretisation effects, directly probing the transport properties of the infinite lattice. It is difficult to achieve error control or computations free from truncation effects via other methods since it can be challenging to predict how large the truncation needs to be *a priori*.

Suppose that the spectrum is located in an interval $[a, b] \subset \mathbb{R}$. We take γ to be a rectangular contour split into four line segments: two parallel to the imaginary axis with real parts $a - 1$ and $b + 1$ and two parallel to the real axis with imaginary parts $\pm\eta$ ($\eta > 0$). Along these line segments we apply Gaussian quadrature with enough quadrature nodes for the desired accuracy (the number of nodes can be found by bounding the analytic integrand). Suppose that the weights and nodes for the quadrature rule applied to the whole of γ are $\{w_j\}_{j=1}^N$ and $\{z_j\}_{j=1}^N$. Then the approximation of (3.14) is given by

$$\psi(t) \approx \sum_{j=1}^N \frac{w_j}{2\pi i} \exp(-iz_j t) [(H - z_j)^{-1}\psi_0]. \quad (3.15)$$

The vectors $(H - z_j)^{-1}\psi_0$ are computed using the adaptive method, which can be performed in parallel across the quadrature nodes. We also reuse these computed vectors for different times t . Numerically, this requires η to not be too large due to the growth of the complex exponential in the complex plane. Suitable N can be selected for a finite interval of desired times t .

4 The Haldane model

In this work, we apply the methods just described to the Haldane model [55]. The Haldane model describes electrons hopping on a two-dimensional honeycomb lattice (Fig. 5) in the presence of a periodic magnetic field with zero net flux. In this section, we first present basic features of the periodic bulk and edge Haldane models and their Bloch reductions in Sections 4.1 and 4.2. We do this only for the reader's convenience since excellent reviews already exist in the literature [47, 76]. We then describe how we model defects and disorder in Section 4.3. We then discuss edge states, and bulk and edge conductances, in Sections 4.4 and 4.5, before making our computational goals more precise in Section 4.6. To improve readability, we postpone some long formulas to Appendix C.

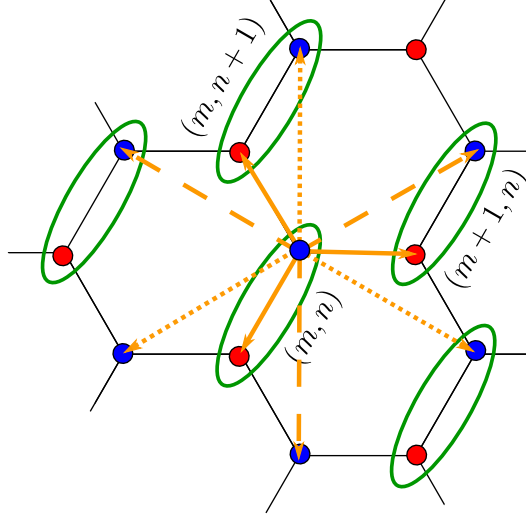


Figure 5: Illustration of hopping terms of the Haldane model (4.1). Red and blue circles denote the A and B sublattices, respectively, and orange lines denote hopping starting at the B site in the (m, n) th cell. Solid orange lines show nearest-neighbour hoppings, while dashed orange lines show next-nearest-neighbour hoppings. Short orange dashes correspond to next-nearest-neighbour hoppings with phase $e^{-i\phi}$, while long orange dashes correspond to next-nearest-neighbour hoppings with phase $e^{i\phi}$.

4.1 The periodic bulk Haldane model

We model electrons in the bulk of the material as elements of the Hilbert space $\ell^2(\mathbb{Z}^2; \mathbb{C}^2)$, written $\psi : \mathbf{m} \mapsto \psi_{\mathbf{m}}$, where $\mathbf{m} = (m, n)$ and $\psi_{\mathbf{m}} = (\psi_{\mathbf{m}}^A, \psi_{\mathbf{m}}^B)^\top$. The quantity $|\psi_{\mathbf{m}}^v|^2$ is then the electron probability density on site $v \in \{A, B\}$ in the \mathbf{m} th cell. The bulk Haldane Hamiltonian H_B is then [55]

$$(H_B \psi)_{\mathbf{m}} := t \begin{pmatrix} \psi_{m,n}^B + \psi_{m-1,n}^B + \psi_{m,n-1}^B \\ \psi_{m,n}^A + \psi_{m+1,n}^A + \psi_{m,n+1}^A \end{pmatrix} + V \begin{pmatrix} \psi_{\mathbf{m}}^A \\ -\psi_{\mathbf{m}}^B \end{pmatrix} + t' \begin{pmatrix} e^{i\phi} (\psi_{m,n+1}^A + \psi_{m-1,n}^A + \psi_{m+1,n-1}^A) + e^{-i\phi} (\psi_{m,n-1}^A + \psi_{m+1,n}^A + \psi_{m-1,n+1}^A) \\ e^{i\phi} (\psi_{m,n-1}^B + \psi_{m+1,n}^B + \psi_{m-1,n+1}^B) + e^{-i\phi} (\psi_{m,n+1}^B + \psi_{m-1,n}^B + \psi_{m+1,n-1}^B) \end{pmatrix}. \quad (4.1)$$

Here, t and $t' \in \mathbb{R}$ are hopping amplitudes between nearest-neighbours and next-nearest-neighbours in the lattice, while $V \in \mathbb{R}$ is a potential difference between sublattices, and $\phi \in [0, 2\pi)$ is the complex phase of the next-nearest-neighbour hopping. Nearest-neighbour and next-nearest-neighbour hoppings are shown in Fig. 5. When $t' \neq 0$ and $\phi \notin \{0, \pi\}$, the next-nearest-neighbour hoppings model a periodic non-zero magnetic flux through the material, whose average over any unit cell is zero.

The bulk Hamiltonian H_B (4.1) is invariant under translations with respect to both components of \mathbf{m} , and can therefore be diagonalised via the Fourier transform [1, 70, 87]. Let $\Gamma^* := [0, 2\pi)^2$, then we write elements of $L^2(\Gamma^*; \mathbb{C}^2)$ as $\hat{\psi} : \mathbf{k} \mapsto \hat{\psi}(\mathbf{k})$, where $\mathbf{k} := (k_1, k_2)$ and $\hat{\psi}(\mathbf{k}) = (\hat{\psi}^A(\mathbf{k}), \hat{\psi}^B(\mathbf{k}))^\top$. We introduce the Fourier transform $\mathcal{F} : \ell^2(\mathbb{Z}^2; \mathbb{C}^2) \rightarrow L^2(\Gamma^*; \mathbb{C}^2)$ and its inverse

$$(\mathcal{F}\psi)(\mathbf{k}) := \sum_{\mathbf{m} \in \mathbb{Z}^2} e^{-i\mathbf{k} \cdot \mathbf{m}} \psi_{\mathbf{m}}, \quad (\mathcal{F}^{-1}\hat{\psi})_{\mathbf{m}} := \frac{1}{|\Gamma^*|} \int_{\Gamma^*} e^{i\mathbf{k} \cdot \mathbf{m}} \hat{\psi}(\mathbf{k}) d\mathbf{k}. \quad (4.2)$$

Under the transformation (4.2), the operator (4.1) takes the form [55]

$$\begin{aligned} ((\mathcal{F}H_B\mathcal{F}^{-1})\hat{\psi})(\mathbf{k}) &= \hat{H}_B(\mathbf{k})\hat{\psi}(\mathbf{k}), \\ \hat{H}_B(\mathbf{k}) &:= \begin{pmatrix} V + t'e^{i\phi}(e^{ik_2} + e^{-ik_1} + e^{i(k_1-k_2)}) + c.c. & t(1 + e^{-ik_1} + e^{-ik_2}) \\ t(1 + e^{ik_1} + e^{ik_2}) & -V + t'e^{i\phi}(e^{-ik_2} + e^{ik_1} + e^{i(k_2-k_1)}) + c.c. \end{pmatrix}, \end{aligned} \quad (4.3)$$

where $+c.c.$ means add the complex conjugate of the term immediately before. Let $E_{\pm}(\mathbf{k})$ denote the ordered eigenvalues of $\hat{H}_B(\mathbf{k})$, known as the Bloch band functions. The spectrum of H_B is then

$$\text{Sp}(H_B) = \text{Sp}_- \cup \text{Sp}_+, \quad \text{Sp}_{\pm} := \bigcup_{\mathbf{k} \in \Gamma^*} E_{\pm}(\mathbf{k}), \quad (4.4)$$

where $E_{\pm}(\mathbf{k})$ is given by an explicit formula (C.1). The associated (non-normalisable) eigenfunctions of H_B are plane wave-like, given explicitly by $\Phi_{\pm}(\mathbf{k}) : \mathbf{m} \mapsto \Phi_{\pm, \mathbf{m}}(\mathbf{k})$, where

$$\Phi_{\pm, \mathbf{m}}(\mathbf{k}) := e^{i\mathbf{k} \cdot \mathbf{m}} \hat{\Phi}_{\pm}(\mathbf{k}), \quad (4.5)$$

and $\hat{\Phi}_{\pm}(\mathbf{k})$ denotes an associated eigenvector of $\hat{H}_B(\mathbf{k})$ with eigenvalue $E_{\pm}(\mathbf{k})$.

4.2 The periodic edge Haldane model

We model electrons at an edge (specifically, a zig-zag edge) of the material as elements ψ in the Hilbert space $\mathcal{H} := \ell^2(\mathbb{N} \times \mathbb{Z}; \mathbb{C}^2)$. The Hamiltonian is again given by (4.1), but we now impose a Dirichlet boundary condition

$$\psi_{-1, n} = 0, \quad n \in \mathbb{Z}. \quad (4.6)$$

We denote the Hamiltonian (4.1) subject to the boundary condition (4.6) by H_E .

The edge Hamiltonian H_E is invariant under translations with respect to n , so it is natural to take a partial Fourier transform. Let $L^2([0, 2\pi); \ell^2(\mathbb{N}; \mathbb{C}^2))$ denote the space of functions $\tilde{\psi} : k \mapsto \tilde{\psi}(k)$, where $\tilde{\psi}(k) : m \mapsto \tilde{\psi}_m(k)$ and $\tilde{\psi}_m(k) = \left(\tilde{\psi}_m^A(k), \tilde{\psi}_m^B(k) \right)^{\top}$, such that $\int_0^{2\pi} \sum_{m=0}^{\infty} |\tilde{\psi}_m(k)|^2 dk < \infty$. We introduce the partial Fourier transform $\mathcal{G} : \ell^2(\mathbb{N} \times \mathbb{Z}; \mathbb{C}^2) \rightarrow L^2([0, 2\pi); \ell^2(\mathbb{N}; \mathbb{C}^2))$ and its inverse

$$(\mathcal{G}\psi)_m(k) := \sum_{n \in \mathbb{Z}} e^{-ikn} \psi_{m, n}, \quad (\mathcal{G}^{-1}\tilde{\psi})_m := \frac{1}{2\pi} \int_0^{2\pi} e^{ikn} \tilde{\psi}_m(k) dk. \quad (4.7)$$

The action of the operator H_E under the transformation (4.7) is then

$$\left((\mathcal{G}H_E\mathcal{G}^{-1}) \tilde{\psi} \right)_m(k) = \left(\hat{H}_E(k) \tilde{\psi}(k) \right)_m, \quad (4.8)$$

where $\hat{H}_E(k)$ is given by (C.3), subject to the boundary condition $\tilde{\psi}_{-1}(k) = 0$. The spectrum of H_E is then

$$\text{Sp}(H_E) = \bigcup_{k \in [0, 2\pi)} \text{Sp}(\hat{H}_E(k)), \quad (4.9)$$

and the associated eigenfunctions are plane wave-like parallel to the edge, given explicitly by $\Phi(k) : \mathbf{m} \mapsto \Phi_{\mathbf{m}}(k)$, where

$$\Phi_{\mathbf{m}}(k) := e^{i\mathbf{k} \cdot \mathbf{m}} \hat{\Phi}_{\mathbf{m}}(k), \quad (4.10)$$

and $\hat{\Phi}(k) : m \mapsto \hat{\Phi}_m(k)$ denotes any eigenfunction of $\hat{H}_E(k)$.

Note that, unlike $\hat{H}_B(\mathbf{k})$, the Bloch-reduced operator in this case, $\hat{H}_E(k)$, generally cannot be diagonalised explicitly. However, we can nonetheless make some general observations. By the Weyl criterion (see Theorem 5.10 of [63]), we clearly have that⁸

$$\text{Sp}(H_B) \subset \text{Sp}(H_E). \quad (4.11)$$

However, equality does not hold in general, because H_E may have additional spectrum due to edge states: (non-normalisable) eigenfunctions (4.10) of H_E arising from the truncation (4.6) which decay rapidly away from the edge [53, 59, 62]. Edge states are closely tied to topological properties of the Haldane model and are discussed in more detail in Section 4.5.

⁸Suppose $\lambda \in \text{Sp}(H_B)$. Then there exists a sequence $\{f_n\} \in \ell^2(\mathbb{Z}^2; \mathbb{C}^2)$ such that $\|f_n\| = 1$ and $\|(H_B - \lambda)f_n\| \rightarrow 0$ as $n \rightarrow \infty$. But since H_E and H_B act identically for $m > 0$, and since H_B is periodic, we can always translate the f_n in order to generate a sequence $\{g_n\} \in \ell^2(\mathbb{N} \times \mathbb{Z}; \mathbb{C}^2)$ such that $\|g_n\| = 1$ and $\|(H_E - \lambda)g_n\| \rightarrow 0$, and hence $\lambda \in \text{Sp}(H_E)$.

4.3 Modeling defects and disorder

We model onsite disorder by adding an additional potential term

$$(V_d\psi)_{\mathbf{m}} = \begin{pmatrix} V_{\mathbf{m}}^A \psi_{\mathbf{m}}^A \\ V_{\mathbf{m}}^B \psi_{\mathbf{m}}^B \end{pmatrix} \quad (4.12)$$

to H_B and H_E , where the $V_{\mathbf{m}}^v$ are independently drawn from a uniform distribution with mean 0 and width w

$$V_{\mathbf{m}}^v \sim \mathcal{U}(0, w), \quad v \in \{A, B\}, \quad \mathbf{m} \in \mathbb{Z}^2. \quad (4.13)$$

Clearly, we have $\|V_d\| \leq w/2$, where $\|\cdot\|$ denotes the operator norm. Note that in this work, we only compute physical properties for individual realisations of disorder; we do not attempt to compute statistical properties over many realisations. We model missing atom defects by setting the wavefunction ψ equal to zero at the missing sites. We write the Hamiltonians H_B and H_E with defects and/or disorder as $H_{B,d}$ and $H_{E,d}$, respectively. Note that $H_{B,d}$ and $H_{E,d}$ cannot be Bloch reduced. To compute their spectral properties, we must work with the infinite-dimensional operators directly.

4.4 Bulk Hall conductance

Physically speaking, eigenfunctions of the operators $H_B, H_E, H_{B,d}$, and $H_{E,d}$ correspond to states that can be occupied by electrons, with energies given by the associated eigenvalues. At zero temperature, there exists a threshold such that every state with energy below the threshold, and no state with energy above the threshold, is occupied by an electron. This threshold is known as the Fermi level. In what follows, we assume that the bands Sp_- and Sp_+ of H_B are separated by a gap, and that the addition of defects and disorder does not close this gap, so that H_B and $H_{B,d}$ have a common gap Δ . We assume further that the Fermi level lies in Δ . Under these assumptions, H_B and $H_{B,d}$ describe (bulk) insulators.

To build intuition, we focus first on the case without defects or disorder. The bulk conductance measures the current excited in the bulk of a material by an applied electric field. The linear coefficient of the conductance can be calculated analytically through linear response theory and is known as the Kubo formula [1, 92]. The part of the conductance parallel to the field vanishes in insulators, but the conductance may have a non-zero transverse (Hall) component. In natural units⁹, and in the limit of zero frequency and dissipation, this component takes the form [102],

$$\sigma_B = \frac{i}{2\pi} \int_{\Gamma^*} \frac{\langle \hat{\Phi}_-(\mathbf{k}) | \partial_{k_1} \hat{H}_B(\mathbf{k}) | \hat{\Phi}_+(\mathbf{k}) \rangle \langle \hat{\Phi}_+(\mathbf{k}) | \partial_{k_2} \hat{H}_B(\mathbf{k}) | \hat{\Phi}_-(\mathbf{k}) \rangle - (1 \leftrightarrow 2)}{(E_+(\mathbf{k}) - E_-(\mathbf{k}))^2} d\mathbf{k}, \quad (4.14)$$

where $(1 \leftrightarrow 2)$ is shorthand for the term immediately before, with 1 replaced everywhere by 2, and vice versa. After a series of manipulations [102], we find

$$\sigma_B = \frac{i}{2\pi} \int_{\Gamma^*} \partial_{k_1} \left\langle \hat{\Phi}_-(\mathbf{k}) \left| \partial_{k_2} \hat{\Phi}_-(\mathbf{k}) \right\rangle - \partial_{k_2} \left\langle \hat{\Phi}_-(\mathbf{k}) \left| \partial_{k_1} \hat{\Phi}_-(\mathbf{k}) \right\rangle d\mathbf{k}. \quad (4.15)$$

The integrand on the right-hand side is the Berry curvature [12] of the $-$ band, and its integral over the Brillouin zone must be an integer multiple of 2π [55, 82, 102]. Thus we have

$$\sigma_B = c_-, \quad (4.16)$$

where c_- is an integer known as the Chern number. The Chern number, being an integer, cannot change value continuously as model parameters are varied and hence remains fixed as long as the bulk gap does not close. The Haldane phase diagram, which describes the values the Chern number can take as the model parameters are varied, can be calculated analytically when the model is periodic [55]. Whenever the Hall conductance is non-zero, we say the model is in its topological phase.

We now consider the case of defects and/or disorder, which prevent Bloch reduction. A convenient expression of the Kubo formula is [2, 43]

$$\sigma_B = -2\pi i \text{Tr} \{ P_B [[P_B, \Lambda_1], [P_B, \Lambda_2]] \}, \quad (4.17)$$

⁹So that the electron charge and Planck's constant both equal 1.

where Tr denotes the trace in $\ell^2(\mathbb{Z}^2; \mathbb{C}^2)$, P_B denotes the spectral projection for the part of the spectrum of $H_{B,d}$ below Δ , Λ_1 and Λ_2 denote characteristic functions for the sets $\{\mathbf{m} \in \mathbb{Z}^2 : m < 0\}$ and $\{\mathbf{m} \in \mathbb{Z}^2 : n < 0\}$, respectively. Note that the operator on the right-hand side of (4.17) is not obviously trace-class. To see that it is, note that Combes–Thomas estimates [36] imply that $[P_B, \Lambda_1]$ acts trivially on sites away from the line $m = 0$, while $[P_B, \Lambda_2]$ acts trivially on sites away from the line $n = 0$. It follows that the operator on the right-hand side of (4.17) acts trivially on sites away from the origin and is hence trace-class.

Finally, although we have so far assumed a spectral gap for $H_{B,d}$ in this section, we expect that definition (4.17) remains valid and is an integer, even when $H_{B,d}$ has no spectral gap, but does exhibit dynamical (Anderson) localisation in a spectral interval, following [43] who proved this in the setting of the quantum Hall effect. Our computational methods do not rely on the existence of a spectral gap, and can be used in this setting as well.

4.5 Edge states, edge conductance, and edge wave-packets

Throughout this section, we continue to assume that H_B and $H_{B,d}$ have a common gap Δ . Recall that it does not follow that Δ is a spectral gap of H_E or $H_{E,d}$, because edge states with energies in the gap may occur.

To build intuition, we again start by considering the periodic setting. Edge states of H_E are extensions (4.10) of bound (normalisable) states associated to discrete eigenvalues $E(k)$ of the operators $\hat{H}_E(k)$ acting on $\ell^2(\mathbb{N}; \mathbb{C}^2)$. As k varies through the interval $[0, 2\pi)$, these eigenvalues sweep out intervals $\text{ran}_{k \in [0, 2\pi)} E(k)$ in the spectrum of H_E (4.9). The maps $E : k \mapsto E(k)$ are known as the dispersion relations of the edge states. Superposing edge states with k values near to some k_0 yields localised wave-packets which propagate along the edge with group velocity given by $E'(k_0)$ [62, 66, 93].

The current carried by edge states with energies in Δ is measured by the edge conductance. More precisely, let Δ' denote any subinterval of Δ , and let $\chi_{\Delta'}$ denote the characteristic function for the interval Δ' . The projection onto edge modes with energies in Δ' is then given by $P_E := \chi_{\Delta'}(H_E)$. In natural units, the edge conductance can then be defined by [66, 93]

$$\sigma_E = \frac{1}{|\Delta'|} \int_0^{2\pi} \tilde{\text{Tr}} \left\{ P_E \partial_k \hat{H}_E(k) \right\} dk, \quad (4.18)$$

where $\tilde{\text{Tr}}$ denotes the trace in $\ell^2(\mathbb{N}; \mathbb{C}^2)$. In the limit where $|\Delta'| \rightarrow 0$ so that $\frac{\chi_{\Delta'}}{|\Delta'|} \rightarrow \delta_\lambda$ for some $\lambda \in \Delta$, σ_E can be computed analytically as follows. Let ν denote the number of edge state dispersion relations which cross λ , assigning +1 to those whose slopes are positive, and −1 to those whose slopes are negative. Then

$$\sigma_E = \nu. \quad (4.19)$$

The principle of bulk-edge correspondence [53, 62, 66, 93] states that $\sigma_B = \sigma_E$, and hence the integer ν equals the bulk Chern number c_- (4.16). A simple consequence of bulk-edge correspondence is that, since $\lambda \in \Delta$ was arbitrary, the edge Hamiltonian H_E must have spectrum filling the whole bulk gap Δ whenever the bulk Chern number is non-zero¹⁰.

In the presence of defects and/or disorder, a convenient expression for the edge conductance in an interval $\Delta' \subset \Delta$ (we assume Δ is again a gap for $H_{B,d}$) is

$$\sigma_E = \frac{-2\pi i}{|\Delta'|} \text{Tr} \{ P_E [H_{E,d}, \Lambda_1] \}, \quad (4.20)$$

where Tr denotes the trace in $\ell^2(\mathbb{N} \times \mathbb{Z}; \mathbb{C}^2)$, $P_E = \chi_{\Delta'}(H_{E,d})$, and Λ_1 again denotes the characteristic function for the set $\{\mathbf{m} \in \mathbb{Z}^2 : m < 0\}$; note that m is the co-ordinate parallel to the edge. Just as with (4.17), it is not immediately obvious that the trace on the right-hand side of (4.20) is well-defined. That it follows from decay of the matrix elements of P_E away from the edge, and of $[H_{E,d}, \Lambda_1]$ away from the line $m = 0$ [43, 66, 67, 93].

Note that, just like the bulk conductance, the edge conductance can be defined and is expected to be quantised, even when $H_{B,d}$ has no spectral gap, but does exhibit dynamical (Anderson) localisation. The definition of the edge conductance in this setting has to be slightly modified from (4.20), however [43]. Our computational methods can easily be generalised to this setting.

¹⁰The spectrum filling the bulk gap is actually absolutely continuous, even in the presence of disorder; see [17].

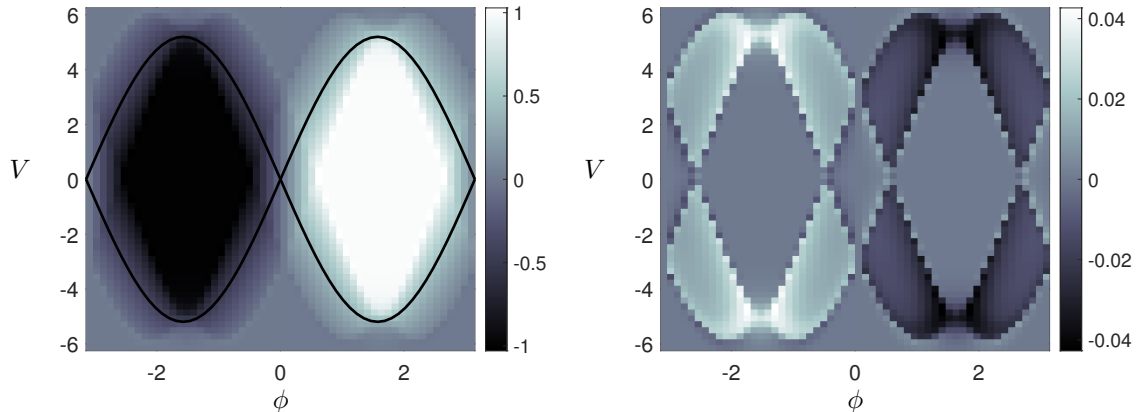


Figure 6: Topological phase plot for $H_{B,d}$ (left panel) with uniform disorder of width $w = 0.2$ (see Section 4.3). The parameters t and t' are fixed at 1 and 0.2, respectively, while V and ϕ are varied. The phase plot for H_B is identical apart from small discrepancies caused by numerical under-resolution along the topological phase boundary; the difference is shown in the right panel. On the left panel we overlay the curves $\pm 3\sqrt{3}t' \sin \phi$ which mark the boundaries of the phase regions computed in the periodic case by Haldane [55].

In the presence of defects and/or disorder, the Bloch decomposition (4.9) is no longer valid. It follows that it no longer makes sense to form edge wave-packets by superposing edge states with nearby wavenumbers, or calculate their group velocities from the edge state dispersion relation. However, the persistence of the edge conductance in this regime suggests that localised initial data with spectral measure concentrated in the bulk gap will still propagate along the edge coherently. This remarkable behaviour has been observed numerically (see, for example, [3, 80]), and even experimentally across various model systems [38, 86, 99, 105]. Such initial data, which we again refer to as edge wave-packets, can be obtained by multiplying approximate edge states, i.e., approximate eigenfunctions of $H_{E,d}$ with energies in the bulk gap, by a smooth decaying function such as a Gaussian.

4.6 Precise statement of TI physical properties to compute

We can now re-state the computational problems (PA)–(PD) referred to in the introduction more precisely.

- (PA) Numerically compute the **bulk** and **edge conductances**, defined for $H_{B,d}$ and $H_{E,d}$ through formulas (4.17) and (4.20), respectively.
- (PB) Numerically compute the **edge states** of H_E and their associated **dispersion relations** $E : k \mapsto E(k)$ by computing the discrete eigenvalues and associated bound states of the Bloch-reduced operators $\hat{H}_E(k)$ (C.3).
- (PC) Numerically compute **approximate edge states** and **edge wave-packets** (defined by multiplying approximate edge states by a smooth, decaying function) of $H_{E,d}$, and their **spectral measures**.
- (PD) Numerically compute the **dynamics** of edge wave-packets of $H_{E,d}$.

5 Results

In this section, we illustrate the utility of our methods by giving several numerical results.

5.1 Bulk and edge conductances

We begin by examining the bulk and edge conductances defined in Sections 4.4 and 4.5, respectively. We compute spectral projections using the method of Section 3.3.

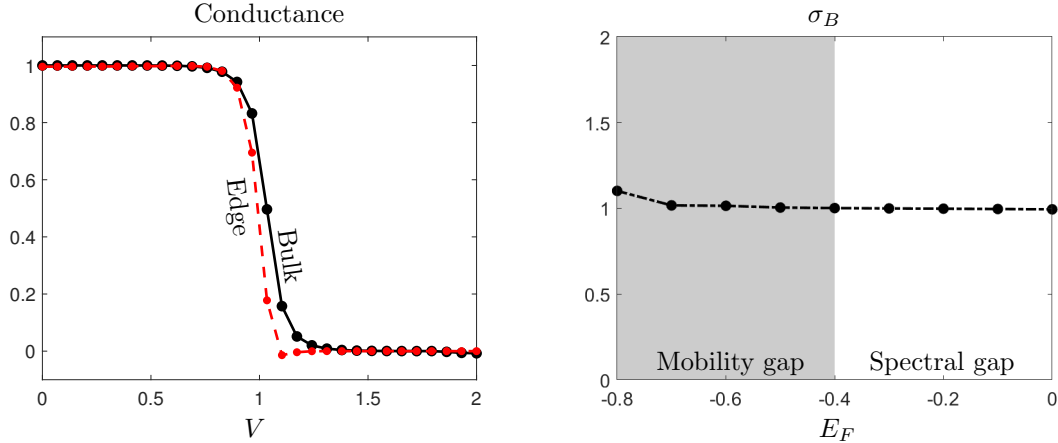


Figure 7: The Bulk and Edge Hamiltonians with parameters $t = 1$, $t' = 0.2$, and $\phi = \pi/2$ exhibit a topological phase transition as V is increased from 0 to 2, during which both the bulk and edge conductance (see (4.17)) switch from 1 to 0 (left panel). When a uniform random potential with $w = 1.8$ (see Section 4.3) is added to H_B , σ_B remains stable as the Fermi level is varied through the spectral gap and regions of the spectrum exhibiting localised eigenstates, which do not support conduction (right panel) [43].

In the left panel of Fig. 6, we show results of numerically computing the bulk Hall conductance of the Haldane model with disorder $H_{B,d}$. In this experiment, the parameters $t = 1$, $t' = 0.2$, and the disorder width $w = 2$ are fixed, while V and ϕ vary. The right panel of Fig. 6 shows the difference between the phase diagram in the left panel and that of H_B , the bulk Haldane model without disorder. The difference is within the chosen numerical tolerance, confirming the stability of the Haldane model’s bulk Hall conductance even in the face of disorder. The computational results are in excellent agreement with the phase diagram computed analytically in Haldane’s original work [55].

The bulk Hall conductance of H_B is plotted as a function of V in the left panel of Fig. 7 and compared with the edge conductance σ_E (see (4.20)). The parameters $t = 1$, $t' = 0.2$, and $\phi = \pi/2$ are fixed in this computation. As V is increased from 0 to 2, both the bulk and edge conductance exhibit a topological phase transition, and switch from 1 to 0. When a uniform random potential with $w = 1.8$ (see Section 4.3) is added to H_B , the spectral gap shrinks. However, the additional spectrum is typically highly localised and we expect that it does not contribute to the conductance. The right panel of Fig. 7 demonstrates that σ_B remains stable even as the Fermi level varies through a spectral gap and a so-called “mobility gap”,¹¹ where the Hamiltonian has spectrum but the associated spectral projection does not contribute to the Hall conductance [43]. Approximate eigenstates of $H_{B,d}$ associated with two spectral regimes are plotted and compared with approximate eigenstates of H_B in Fig. 8. The states associated with the mobility gap are highly localised and do not contribute to conductance (see (8), bottom), while the states corresponding to points in the spectrum of H_B are not localised (see Fig. 8, top).

5.2 Edge states at a periodic edge and their dispersion relations

We now show results of computing edge states and their dispersion relations, as discussed in Section 4.5. To do this, we compute the spectrum and associated eigenfunctions (when the spectrum is discrete) of the infinite-dimensional operators $\hat{H}_E(k)$ (C.3) using the methods of Section 3.1.

We start by computing the spectrum of the operators $\hat{H}_E(k)$ (C.3) for $k \in [0, 2\pi)$, showing the results in Fig. 9. We select the parameters $t = 1$, $t' = 0.1$, $\phi = \pi/2$ and $V = 0.2$, for which the model is in its topological phase and hence edge states must occur. The spectrum consists of two parts. The first part is the spectrum of H_B (4.1) after Bloch-reduction with respect to one of the quasi-momenta, and is marked in black on Fig. 9. The second part is the additional part of the spectrum arising from the Dirichlet boundary condition at the edge (4.6), and is marked in blue on Fig. 9. For any fixed k ,

¹¹Here we use the convenient terminology “mobility gap” to refer to an interval where the Hamiltonian has spectrum but the associated spectral projection does not contribute to conduction. We are not aware of any rigorous result proving existence of such a regime for the Haldane model, although such a regime is known to occur in models of the quantum Hall effect [50].

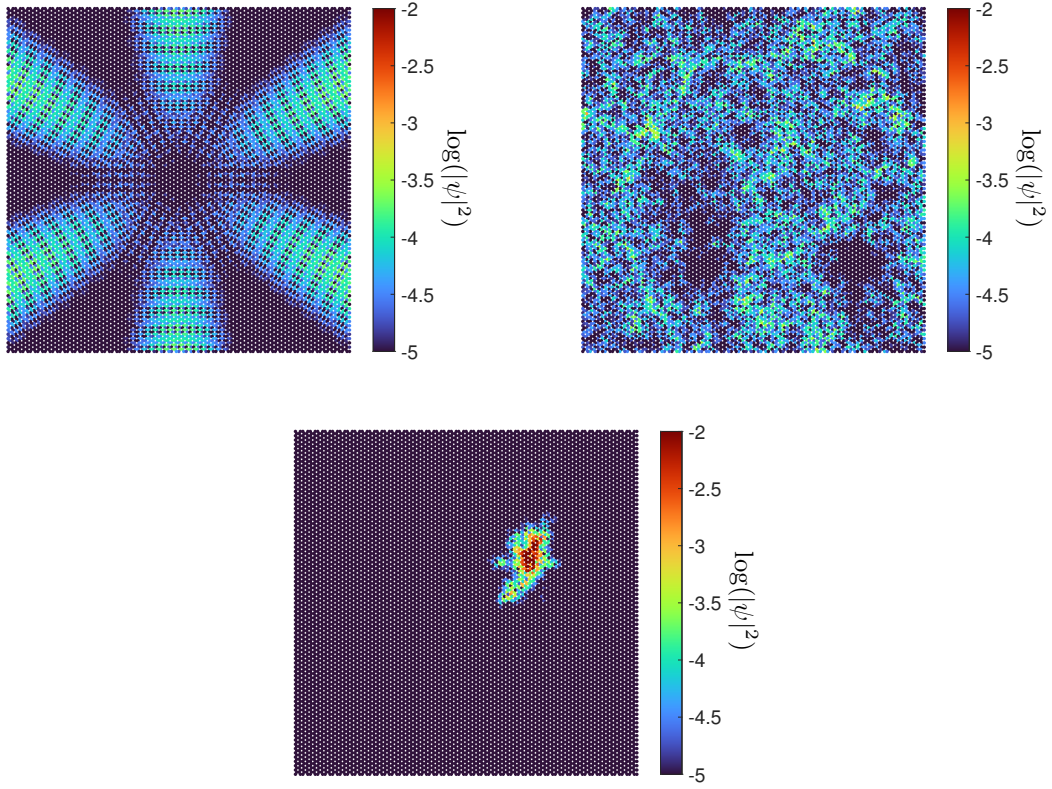


Figure 8: Approximate eigenstate of H_B with parameters $t = 1$, $t' = 0.2$, $\phi = \pi/2$ associated with point -1.5 in $\text{Sp}(H_B)$ (top left). The approximate eigenstate has rotational symmetry because it is computed using rectangular truncations in the radial direction. Approximate eigenstates of $H_{B,d}$ with $w = 1.8$ associated with points -1.5 (top right) and -0.6 (bottom) in $\text{Sp}(H_{B,d})$. We show a truncated square portion of the computed approximate state in each case.

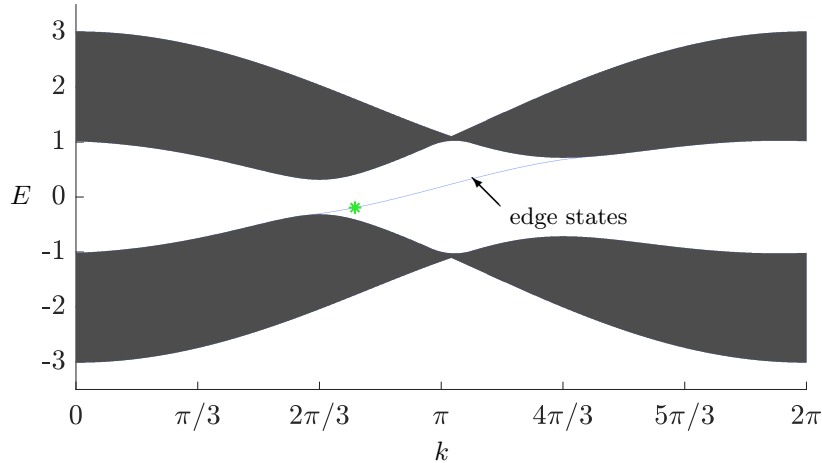


Figure 9: Plot of the spectra of the Bloch-reduced edge Hamiltonian operators $\hat{H}_E(k)$ (C.3) as a function of $k \in [0, 2\pi)$. The spectrum of H_E (4.6) is the union of these spectra. The black portion of the plot corresponds to the spectrum of the bulk Hamiltonian H_B (4.1) after Bloch-reduction in the direction parallel to the edge. The blue portion corresponds to spectrum resulting from the Dirichlet boundary condition at the edge (4.6). The green star corresponds to the edge state in Fig. 10 (left). Note that we choose to consider an edge state whose energy is close to the bulk spectrum, which makes coupling of the edge state to bulk modes possible in Fig. 15 and Fig. 16. For each value of k we adaptively increased the truncation size until the error in (3.2) was below the chosen tolerance 0.01.

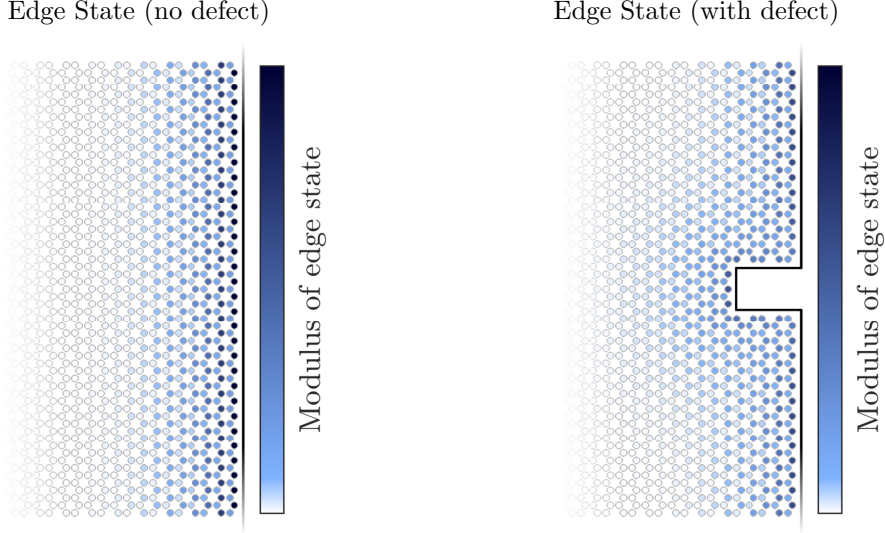


Figure 10: Left: Absolute value of the approximate eigenstate (periodically continued to the whole lattice) of the edge Hamiltonian corresponding to the green star in Fig. 9. We have truncated the lattice to show only a finite portion. Right: An edge state at the energy of the green star when we have an additional defect of missing sites.

this spectrum is discrete, with an associated eigenfunction that decays into the bulk. The associated eigenfunctions of these eigenvalues are known as edge states. When extended according to (4.10) they become non-normalisable eigenfunctions of H_E that extend parallel to the edge. We plot an extended edge state, corresponding to the green star marked in Fig. 9, in the left panel of Fig. 10. Before extension to the whole lattice, the computed state has a residual of less than 4×10^{-16} .

5.3 Approximate edge states at a non-periodic edge

Next, we show results of computing approximate edge states non-periodic edges. Since the edge Hamiltonian cannot be Bloch reduced, we must compute edge states through the infinite-dimensional Hamiltonian directly. Since the spectrum associated to edge states is absolutely continuous [17], we restrict attention to computing *approximate* edge states using the methods of Section 3.1.

Our first experiment seeks to answer the question: *What happens to the edge state in Fig. 9 if we remove a group of sites along the edge?* More specifically, what is the form of the approximate edge state of the edge Hamiltonian with the defect $H_{E,d}$, with the same energy as that exact edge state? This mode is computed in the right panel of Fig. 10 with residual bounded by 10^{-3} (this residual is larger than for the periodic case in Section 5.2 since we must compute an edge state that does not decay parallel to the edge through the infinite-dimensional Hamiltonian directly). The approximate edge state simply snakes around the defect. Away from the defect, the approximate edge state of $H_{E,d}$ is essentially identical to the exact edge state of H_E . This is quite a general phenomenon: in Fig. 11, we compare the diagonal entries of the spectral projections onto an interval of edge states of the edge Hamiltonians with and without missing atoms. We find that the difference in the projections decays rapidly away from the defect.

Our second experiment considers the same question, but in this case the perturbation is no longer a local defect of the edge, but a random onsite potential (4.12) added to every site with $w = 1$. This potential represents a non-compact perturbation of H_E . We plot the value of the specific realisation of the random potential used for our experiment in the left panel of Fig. 12. In the right panel of Fig. 12 we plot the approximate edge state with a residual bounded by 10^{-3} . We find that the approximate edge state persists again, despite the perturbation.

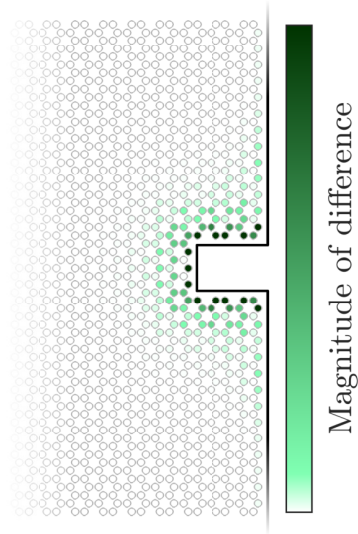


Figure 11: Using the method of Section 3.3, we can compute spectral projections onto an interval Δ of edge states of H_E and $H_{E,d}$, where $H_{E,d}$ has sites removed from the edge, in order to visualise how the whole interval of edge states responds to the perturbation. The selected parameters are $t = 1$, $t' = 0.1$, $\phi = \pi/2$ and $V = 0.2$. Here, we compute the spectral projections onto edge states associated with the interval $[-0.1, 0.05]$ and plot the difference of the diagonal entries of these projections. We see that the defect only affects the projection locally, i.e., near the missing atoms.

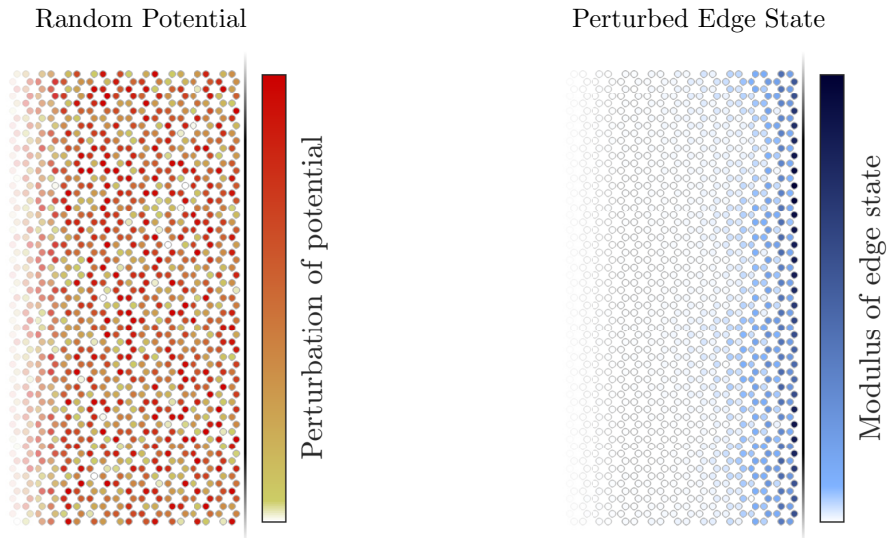


Figure 12: Left: Specific realisation of the random potential (4.12), added at every site. Right: The approximate edge state of $H_{E,d}$ with the same energy as edge state shown in left panel of Fig. 10.

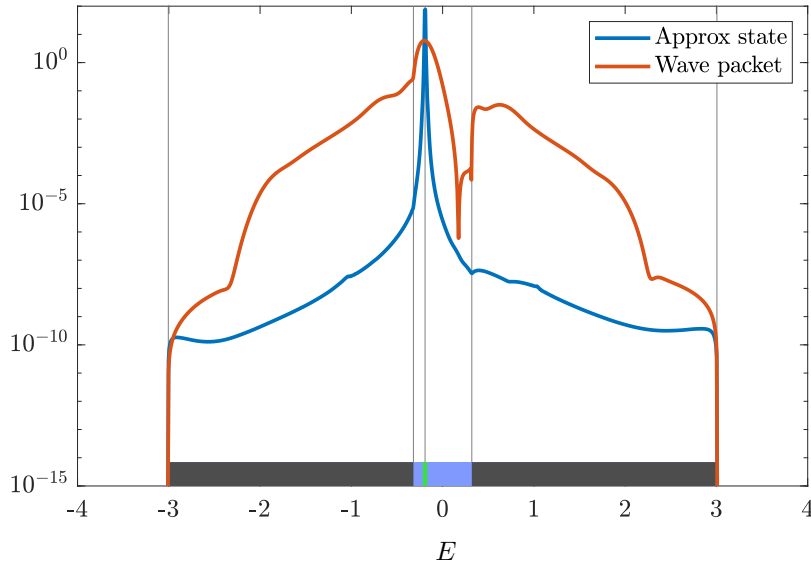


Figure 13: The (smoothed) spectral measure of an approximate eigenstate and a wave packet. The spectrum of the Hamiltonian is plotted at the bottom with vertical grey lines added for clarity. The approximate state was computed at the green energy. Notice the log scale on the vertical axis. The spectral measure of the edge wave-packet is much more spread out, as expected, with non-trivial support on the bulk spectrum.

5.4 Edge wave-packets and spectral measure

We now compute edge wave-packets and investigate their spectral measures using the methods of Section 3.2. We start by computing the spectral measure of the approximate edge state in the right panel of Fig. 10. This is depicted in blue in Fig. 13, where we used a sixth-order kernel with smoothing parameter $\epsilon = 0.01$. The truncation parameter is selected adaptively for each spectral parameter as outlined in Section 3.2. We see that, as expected, the spectral measure is heavily weighted around the energy at which we computed the approximate edge state. Next, we look at the spectral measure when we create a wave packet out of this approximate eigenstate. To create the wave-packet, we multiply the approximate eigenstate by a Gaussian centred away from the defect. This multiplication is equivalent to convolving the approximate edge state by a Gaussian in momentum space. Therefore, the spectral measure of the wave-packet will be spread out compared to the spectral measure of the approximate edge state. The orange part of the plot confirms this expected behaviour. We have repeated this process for the state shown in the right panel of Fig. 12, but we omit these results since they are similar to those shown in Fig. 13.

We can probe how the spectral properties of the edge Hamiltonian change when the random potential (4.12) is added by computing the spectral measures of a delta function at a single site on the edge¹², with and without the random potential. The results are shown in Fig. 14 for $t = 1$, $t' = 0.1$, $\phi = \pi/2$, $V = 0.2$ and $w = 1$. We observe that the potential causes the spectral measure to become significantly more singular in the bulk spectrum, while the edge spectrum changes shape but remains smooth. This is consistent with absolute continuity of the edge spectral measure [17], but we are not aware of work which would explain the behavior of the bulk spectral measure.

5.5 Time propagation of edge wave-packets

Finally, we look at the time propagation of wave packets along the edge for $t = 1$, $t' = 0.1$, $\phi = \pi/2$ and $V = 0.2$. We begin with a wave packet produced as in the previous subsection – by computing an approximate edge state and multiplying by a Gaussian far from (above) the defect. Due to the positive slope of the edge spectrum in Fig. 9, we expect that the edge states will move down the edge. Additionally, since the edge states of the edge Hamiltonian with sites removed are similar to

¹²The spectral measure for edge wave-packets with added random disorder behave similarly to Fig. 13.

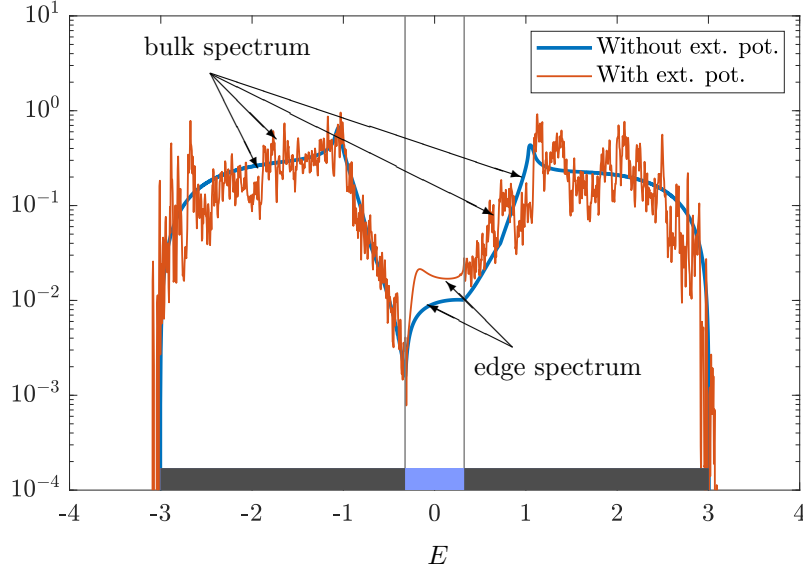


Figure 14: The (smoothed) spectral measure of a site along the zig-zag edge. The boundaries of the edge spectrum of the Hamiltonian without the external potential are shown as vertical grey lines added for clarity. Notice that the addition of the random potential causes a more singular spectral measure on the bulk spectrum, but the spectral measure on the edge spectrum remains smooth.

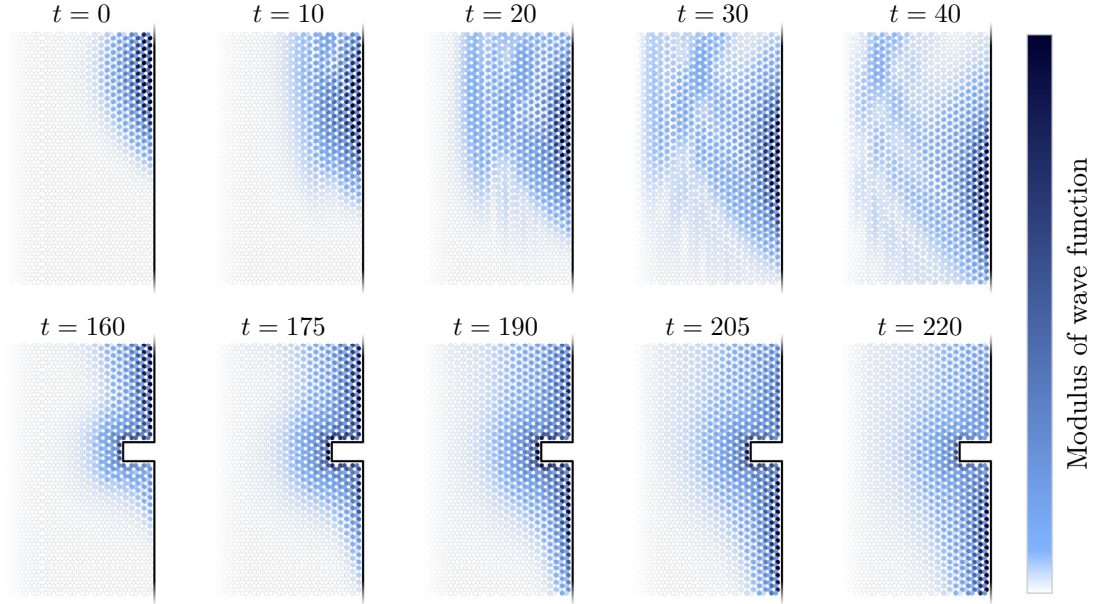


Figure 15: Time propagation of a wave packet. Top left is the initial state (a wave packet far away from a defect). The images go forward in time as we move to the right. We observe the wave-packet clearly losing mass to bulk modes. Then we fast forward to the bottom left (and move our camera down) to see the remaining wave packet just starting to hit the defect. The wave packet then crawls around the defect as we go to the right. Note that (essentially) no further mass is lost to bulk modes as the wave-packet propagates around the defect.

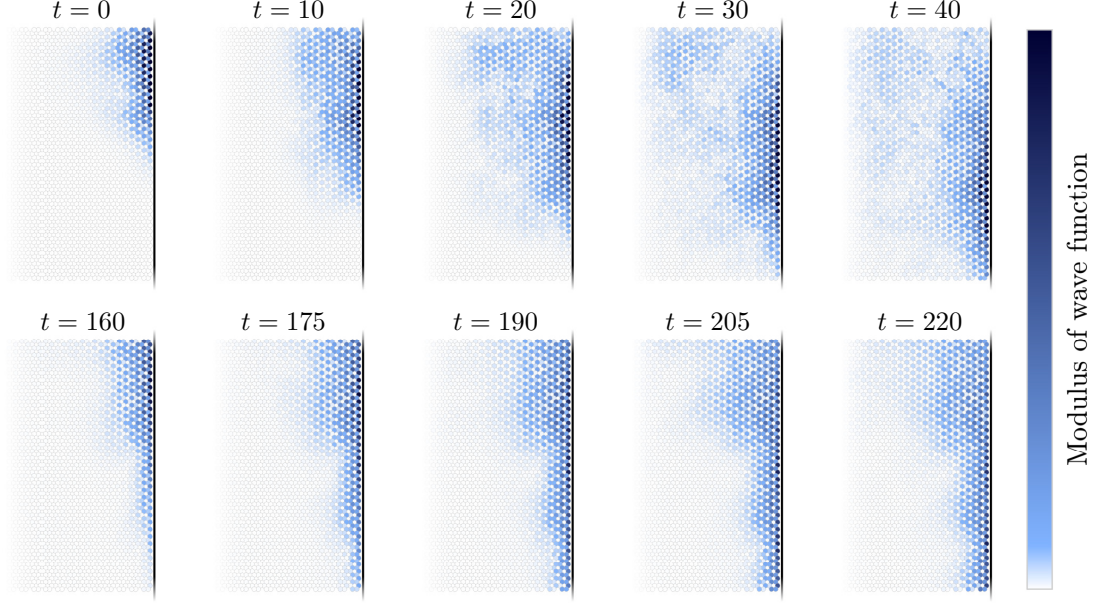


Figure 16: The propagation of a wave packet in a system with a random perturbation to the external potential at every site. Again, top left is the initial state and time goes forward as we move to the right. Then we fast forward (and move our camera down) to get to the bottom left picture. What is left of the wave packet then continues to propagate. Just as in Fig. 15, we observe loss of mass to bulk modes at the beginning of the simulation, and very little afterwards.

the unperturbed edge state, we expect them to behave similarly. Lastly, by looking at the spectral measure of a wave packet in the previous subsection, we expect that some of the density of the wave packet will be lost to the bulk. However, most of it will continue along the edge.

We compute the time evolution with a relative ℓ^2 error bound of 10^{-5} . Fig. 15 shows the results. In the beginning, we observe part of the wave packet propagating into the bulk. This propagation is consistent with our computation of the spectral measure in Fig. 13, which showed that the wave packet has non-trivial spectral support among bulk modes. Interestingly, the remaining wave packet remains very coherent as it propagates around the defect, with little further coupling to the bulk. This is consistent with our computation of an approximate edge state of the model with defect, Fig. 10, which showed the edge state snaking around the defect similarly to the edge state without a defect, and with our computation of the spectral measure in Fig. 13, which showed that the wave packet is primarily concentrated among such edge states.

We perform a similar test with a Hamiltonian that has disorder everywhere. Namely, we add a random potential described in Section 5.2 at each site with $w = 1$. Fig. 16 shows the results. Again, we observe part of the wave packet propagating to the bulk and then generally coherent propagation along the edge.

A Pseudocode for the algorithms

Algorithm 1 Computation of spectrum and the associated approximate states with error control via the method of [35]. The computation of \tilde{F}_n can be performed in parallel.

Input: \tilde{H} , f , n and G_n (with resolution $r_n \geq 1$).

- 1: For each $z \in G_n$, compute $\tilde{F}_n(z) = \lceil 2r_n F_n(z) \rceil / (2r_n)$ and $v_n(z)$, the right-singular vector of $P_{f(n)}(\tilde{H} - z)P_n$ corresponding to the smallest singular value.
- 2: For $z \in G_n$, if $\tilde{F}_n(z) \leq 1/2$, then set

$$I_z = \left\{ w \in G_n : |w - z| \leq \tilde{F}_n(z) \right\}, \quad M_z = \left\{ w \in G_n : \tilde{F}_n(w) = \min_{x \in I_z} \tilde{F}_n(x) \right\}.$$

Otherwise, set $M_z = \emptyset$.

Output: $\Gamma_n = \cup_{z \in G_n} M_z$ (approximation of spectrum), $E_n = \max_{z \in \Gamma_n} \tilde{F}_n(z)$ (error bound) and $V_n = \cup_{z \in \Gamma_n} \{v_n(z)\}$ (approximate states).

Algorithm 2 A practical framework for evaluating an approximate spectral measure of an operator \tilde{H} at $x_0 \in \mathbb{R}$ with respect to a vector $\psi \in \mathcal{H}$ via the method of [25, 34]. For the examples of this paper, the resolvent is computed using the rectangular truncations in (2.1). However, the framework generalises to arbitrary self-adjoint operators given the ability to approximate solutions of the shifted linear systems and inner products.

Input: \tilde{H} , $\psi \in \mathcal{H} \cong l^2(\mathbb{N})$, $x_0 \in \mathbb{R}$, $a_1, \dots, a_m \in \{z \in \mathbb{C} : \text{Im}(z) > 0\}$, and $\epsilon > 0$.

- 1: Solve the Vandermonde system (3.7) for the residues $\alpha_1, \dots, \alpha_m \in \mathbb{C}$.
- 2: Solve $(\tilde{H} - (x_0 - \epsilon a_j))u_j^\epsilon = \psi$ for $1 \leq j \leq m$.
- 3: Compute $\mu_\psi^\epsilon(x_0) = \frac{-1}{\pi} \text{Im} \left(\sum_{j=1}^m \alpha_j \langle u_j^\epsilon, \psi \rangle \right)$.

Output: $\mu_\psi^\epsilon(x_0)$.

Algorithm 3 An efficient method (see Section 3.3) to compute spectral projections associated with the projection-valued measure \mathcal{E} of an operator \tilde{H} .

Input: \tilde{H} , $\psi \in \mathcal{H} \cong l^2(\mathbb{N})$, $[a, b] \subset \mathbb{R}$, $\theta_1, \dots, \theta_N \in [0, 1]$, $w_1, \dots, w_N \in \mathbb{R}_+$, $a_1, \dots, a_m \in \{z \in \mathbb{C} : \text{Im}(z) > 0\}$, and $\epsilon > 0$.

- 1: Solve the Vandermonde system (3.7) for the residues $\alpha_1, \dots, \alpha_m \in \mathbb{C}$.
- 2: Set $z_\ell = a + \frac{b-a}{2}(1 + \exp(\pi i \theta_\ell))$ and $z'_\ell = -i \frac{b-a}{2} \exp(\pi i \theta_\ell)$.
- 3: Solve $(\tilde{H} - (z_\ell - \epsilon a_j))u_j^\epsilon = \psi$ and $(\tilde{H} - (\bar{z}_\ell - \epsilon \bar{a}_j))v_j^\epsilon = \psi$ for $1 \leq j \leq m$, and each $1 \leq \ell \leq N$.
- 4: Solve $(\tilde{H} - a \mp i\epsilon)u_{a,\pm}^\epsilon = \psi$ and $(\tilde{H} - b \mp i\epsilon)u_{b,\pm}^\epsilon = \psi$.
- 5: Compute $\mathcal{E}_{(a,b)}^\epsilon \psi = \frac{-1}{2\pi i} \sum_{\ell=1}^N \sum_{j=1}^m w_\ell [\alpha_j z'_\ell u_j^\epsilon - \bar{\alpha}_j \bar{z}'_\ell v_j^\epsilon] - \frac{\epsilon}{2i} \left(c_l [u_{a,+}^\epsilon - u_{a,-}^\epsilon] + c_r [u_{b,+}^\epsilon - u_{b,-}^\epsilon] \right)$.

Output: $\mathcal{E}_{(a,b)}^\epsilon \psi$.

B Convergence for smoothed projection-valued measures

In this appendix, we prove Theorem 3.2. We begin by establishing convergence and calculating the endpoint contributions c_l and c_r for rational kernels with conjugate pole pairs.

Proposition B.1. *Given a projection-valued measure \mathcal{E} (see (3.3)) and m th order kernel K with conjugate pole pairs (see (3.8)), then for any $[a, b] \subset \mathbb{R}$, we have that*

$$\lim_{\epsilon \rightarrow 0^+} \int_a^b [K_\epsilon * \mathcal{E}](x) dx = \mathcal{E}((a, b)) + c_l \mathcal{E}(\{a\}) + c_r \mathcal{E}(\{b\}),$$

m	$\pi K(x) \prod_{j=1}^m (x - a_j)(x - \bar{a}_j)$	$\{\alpha_1, \dots, \alpha_{\lceil m/2 \rceil}\}$
2	$\frac{20}{9}$	$\left\{\frac{1+3i}{2}\right\}$
3	$-\frac{5}{4}x^2 + \frac{65}{16}$	$\{-2+i, 5\}$
4	$-\frac{3536}{625}x^2 + \frac{21216}{3125}$	$\left\{\frac{-39-65i}{24}, \frac{17+85i}{8}\right\}$
5	$\frac{130}{81}x^4 - \frac{12350}{729}x^2 + \frac{70720}{6561}$	$\left\{\frac{15-10i}{4}, \frac{-39+13i}{2}, \frac{65}{2}\right\}$
6	$\frac{1287600}{117649}x^4 - \frac{34336000}{823543}x^2 + \frac{667835200}{40353607}$	$\left\{\frac{725+1015i}{192}, \frac{-2775-6475i}{192}, \frac{1073+7511i}{96}\right\}$

Table 1: The numerators and residues of the first six rational kernels with equispaced poles. We give the first $\lceil m/2 \rceil$ residues because the others follow by the symmetry $\alpha_{m+1-j} = \bar{\alpha}_j$.

where $c_l = \pi^{-1} \sum_{j=1}^m \beta_j (\pi - \arg(a_j)) + i\gamma_j \log |a_j|$ and $c_r = \pi^{-1} \sum_{j=1}^m \beta_j \arg(a_j) - i\gamma_j \log |a_j|$.

Proof. First, integrate both sides of (3.10) over the interval, substitute the resolvent identity in (3.4) on the right-hand side, and apply Fubini's theorem to obtain

$$\int_a^b [K_\epsilon * \mathcal{E}](x) dx = \frac{-1}{2\pi i} \int_{\text{Sp}(H)} \int_a^b \sum_{j=1}^m \left[\frac{\alpha_j}{\lambda - (x - \epsilon a_j)} - \frac{\bar{\alpha}_j}{\lambda - (x - \epsilon \bar{a}_j)} \right] dx d\mathcal{E}(\lambda).$$

To establish the theorem, we take the limit $\epsilon \rightarrow 0$ and apply the dominated convergence theorem to interchange the limit and the outer integral. This is permissible due to the decay condition in part (iii) of Theorem 3.1. We claim that, as $\epsilon \rightarrow 0$, the inner integral converges to $-2\pi i$ when $\lambda \in (a, b)$, 0 when $\lambda \notin [a, b]$, and $(-2\pi i)c_l$ or $-(2\pi i)c_r$ when $\lambda = a$ or $\lambda = b$, respectively.

We compute the inner integral directly by integrating the sum term by term, so that

$$\int_a^b \sum_{j=1}^m \left[\frac{\alpha_j}{\lambda - (x - \epsilon a_j)} - \frac{\bar{\alpha}_j}{\lambda - (x - \epsilon \bar{a}_j)} \right] dx = \sum_{j=1}^m [\bar{\alpha}_j \log(\lambda - (x - \epsilon \bar{a}_j)) - \alpha_j \log(\lambda - (x - \epsilon a_j))] \Big|_a^b.$$

Using the identity $\log(z) = \log|z| + i \arg(z)$ to simplify, we find that the right-hand side is equal to

$$2 \sum_{j=1}^m \text{Im}(\alpha_j) [\log|\lambda - b + \epsilon a_j| - \log|\lambda - a + \epsilon a_j|] - i \text{Re}(\alpha_j) [\arg(\lambda - b + \epsilon a_j) - \arg(\lambda - a + \epsilon a_j)]. \quad (\text{B.1})$$

To calculate the limit, note that the first row of (3.7) states that $\sum_{j=1}^m \alpha_j = 1$. In particular, $\sum_{j=1}^m \text{Re}(\alpha_j) = 1$ and $\sum_{j=1}^m \text{Im}(\alpha_j) = 0$. Then, the right-hand terms involving \arg evaluate to

$$\lim_{\epsilon \rightarrow 0} \sum_{j=1}^m \text{Re}(\alpha_j) [\arg(\lambda - b + \epsilon a_j) - \arg(\lambda - a + \epsilon a_j)] = \begin{cases} \pi, & a < \lambda < b, \\ \sum_{j=1}^m \text{Re}(\alpha_j) (\pi - \arg(a_j)), & \lambda = a, \\ \sum_{j=1}^m \text{Re}(\alpha_j) \arg(a_j), & \lambda = b, \\ 0, & \text{otherwise.} \end{cases} \quad (\text{B.2})$$

On the other hand, the left-hand terms involving logarithms vanish when $\lambda \neq a$ and $\lambda \neq b$, that is,

$$\lim_{\epsilon \rightarrow 0} \sum_{j=1}^m \text{Im}(\alpha_j) [\log|\lambda - b + \epsilon a_j| - \log|\lambda - a + \epsilon a_j|] = [\log|\lambda - b| - \log|\lambda - a|] \sum_{j=1}^m \text{Im}(\alpha_j) = 0. \quad (\text{B.3})$$

Finally, when $\lambda = b$ we expand $\log|\epsilon a_j| = \log|\epsilon| + \log|a_j|$ and perform a similar calculation to obtain

$$\lim_{\epsilon \rightarrow 0} \sum_{j=1}^m \text{Im}(\alpha_j) [\log|\epsilon a_j| - \log|b - a + \epsilon a_j|] = \sum_{j=1}^m \text{Im}(\alpha_j) \log|a_j|. \quad (\text{B.4})$$

We omit the analogous calculation for $\lambda = a$, which only differs by a minus sign. Collecting the results in (B.1), (B.2), (B.3) and (B.4) establishes the claim and concludes the proof the proposition. \square

In practice, we usually employ symmetric rational kernels whose poles have reflection symmetry over the imaginary axis. In this case, the residues are symmetric over the real axis, and the constants c_l and c_r simplify considerably. These statements are made precise in the next two lemmas.

Lemma B.2. *If the poles satisfy $a_{m+1-j} = -\bar{a}_j$, then the residues satisfy $\alpha_{m+1-j} = \bar{\alpha}_j$.*

Proof. We proceed by calculating the residues directly from the Vandermonde system in (3.7). By Cramer's rule, $\alpha_j = \det(V_j)/\det(V)$, where V is the transposed Vandermonde matrix and V_j is identical except that the j th column is replaced by the unit vector on the right-hand side of (3.7). We claim that $\det(V)$ is real and $\det(V_{m+1-j}) = \det(V_j)$, which together imply that $\alpha_{m+1-j} = \bar{\alpha}_j$.

The determinant of V is given by the well-known formula $\det(V) = \prod_{1 \leq i < j \leq m} (a_j - a_i)$. Pairing conjugate terms and noting that $(a_{m+1-i} - a_{m+1-j}) = (\bar{a}_j - \bar{a}_i)$ by the reflection symmetry hypothesis, we find that the determinant is real because

$$\det(V) = \prod_{1 \leq i < j \leq m} (a_j - a_i) = \prod_{1 \leq i < j \leq \lceil m/2 \rceil} (a_j - a_i)(a_{m+1-i} - a_{m+1-j}) = \prod_{1 \leq i < j \leq \lceil m/2 \rceil} |a_j - a_i|^2.$$

To calculate the determinant of V_j , note that a Laplace expansion down the j th column yields

$$\det(V_j) = (-1)^{j-1} \begin{vmatrix} a_1 & \dots & a_{j-1} & a_{j+1} & \dots & a_m \\ \vdots & & \vdots & \vdots & & \vdots \\ a_1^{m-1} & \dots & a_{j-1}^{m-1} & a_{j+1}^{m-1} & \dots & a_m^{m-1} \end{vmatrix} = (-1)^{j-1} \prod_{\substack{1 \leq i \leq m, \\ i \neq j}} a_i \prod_{\substack{1 \leq i < k \leq m, \\ i, k \neq j}} (a_k - a_i). \quad (\text{B.5})$$

The second equality follows by factoring the poles $a_1, \dots, a_{j-1}, a_{j+1}, \dots, a_m$ out of their respective columns and applying the formula for the determinant of the resulting $(m-1) \times (m-1)$ Vandermonde system (note that the indices are $1, \dots, j-1, j+1, \dots, m$). Since the poles are distinct, we may write

$$\prod_{\substack{1 \leq i < k \leq m, \\ i, k \neq j}} (a_k - a_i) = \det(V) \left(\prod_{1 \leq i < j} (a_j - a_i) \prod_{j < i \leq m} (a_i - a_j) \right)^{-1}. \quad (\text{B.6})$$

Applying the reflection symmetry hypothesis and re-indexing with $i' = m+1-i$, we calculate that

$$\prod_{1 \leq i < j} (a_j - a_i) \prod_{j < i \leq m} (a_i - a_j) = \prod_{1 \leq i' < m+1-j} (\bar{a}_{m+1-j} - \bar{a}_{i'}) \prod_{m+1-j < i' \leq m} (\bar{a}_{i'} - \bar{a}_{m+1-j}). \quad (\text{B.7})$$

Since $\det(V)$ is real-valued, it follows that $\prod_{\substack{1 \leq i < k \leq m, \\ i, k \neq j}} (a_k - a_i) = \prod_{\substack{1 \leq i < k \leq m, \\ i, k \neq m+1-j}} \overline{(a_k - a_i)}$. Similarly,

$$\prod_{\substack{1 \leq i \leq m, \\ i \neq j}} a_i = (a_j)^{-1} \prod_{1 \leq i \leq m} a_i = (-\bar{a}_{m+1-j})^{-1} \prod_{1 \leq i \leq m} (-\bar{a}_{m+1-i})^{-1} = (-1)^{m+1} \prod_{\substack{1 \leq i \leq m, \\ i \neq m+1-j}} \bar{a}_i. \quad (\text{B.8})$$

Compiling the calculations in (B.5), (B.6), (B.7), and (B.8) establishes the claim, as we conclude that

$$\det(V_j) = (-1)^{j-1} \prod_{\substack{1 \leq i \leq m, \\ i \neq j}} a_i \prod_{\substack{1 \leq i < k \leq m, \\ i, k \neq j}} (a_k - a_i) = (-1)^{m-j} \prod_{\substack{1 \leq i \leq m, \\ i \neq m+1-j}} \bar{a}_i \prod_{\substack{1 \leq i < k \leq m, \\ i, k \neq m+1-j}} \overline{(a_k - a_i)} = \overline{\det(V_{m+1-j})}.$$

Therefore, Cramer's rule implies that the residues satisfy $\alpha_{m+1-j} = \bar{\alpha}_j$, for each $j = 1, \dots, m$. \square

With the conjugate symmetry of the residues in hand, we can now show that the constants in Theorem B.1 simplify significantly for symmetric kernels. Recall that $\sum_{j=1}^m \beta_j = 1$ and $\sum_{j=1}^m \gamma_j = 0$.

Lemma B.3. *If the poles satisfy $a_{m+1-j} = -\bar{a}_j$, then $c_l = c_r = 1/2$ in Theorem B.1.*

Proof. To begin, note that symmetry of the residues over the real axis in Theorem B.2 implies that $\gamma_{m+1-j} = -\gamma_j$, while the symmetry of the poles over the imaginary axis implies that $\log |a_j| = \log |a_{m+1-j}|$. Therefore, the logarithmic terms in c_l and c_r vanish because¹³

$$\sum_{j=1}^m \gamma_j \log |a_j| = \sum_{j=1}^{\lceil m/2 \rceil} (\gamma_j \log |a_j| + \gamma_{m+1-j} \log |a_{m+1-j}|) = 0.$$

¹³When m is odd, the relation $\gamma_{m+1-j} = -\gamma_j$ holds for $j = \lceil m/2 \rceil$, so that $\gamma_{\lceil m/2 \rceil} = 0$.

Furthermore, the pole symmetries $a_{m+1-j} = -\bar{a}_j$ imply that $\arg(a_{m+1-j}) = \pi - \arg(a_j)$, while the residue symmetries also imply that $\beta_{m+1-j} = \beta_j$. Therefore, we find that

$$c_l = \pi^{-1} \sum_{j=1}^m \beta_j (\pi - \arg(a_j)) = \pi^{-1} \sum_{j=1}^m \beta_j \arg(a_j) = c_r. \quad (\text{B.9})$$

Now, observe that $\beta_j \arg(a_j) + \beta_{m+1-j} \arg(a_{m+1-j}) = \pi \beta_j$. For even m , we calculate that

$$\sum_{j=1}^m \beta_j \arg(a_j) = \sum_{j=1}^{m/2} (\beta_j \arg(a_j) + \beta_{m+1-j} \arg(a_{m+1-j})) = \pi \sum_{j=1}^{m/2} \beta_j = \frac{\pi}{2}, \quad (\text{B.10})$$

The last equality follows from the fact that $2 \sum_{j=1}^{m/2} \beta_j = \sum_{j=1}^m \beta_j = 1$ when m is even. Analogously for odd m , we obtain

$$\sum_{j=1}^m \beta_j \arg(a_j) = \frac{\pi}{2} \beta_{\lceil m/2 \rceil} + \pi \sum_{j=1}^{\lfloor m/2 \rfloor} \beta_j = \frac{\pi}{2}. \quad (\text{B.11})$$

Here, we have used that $\beta_{\lceil m/2 \rceil} + 2 \sum_{j=1}^{\lfloor m/2 \rfloor} \beta_j = \sum_{j=1}^m \beta_j = 1$ when m is odd. Plugging (B.10) and (B.11) into (B.9) demonstrates that $c_l = c_r = 1/2$, which concludes the proof. \square

C Haldane model details

In this section, we fill in some details omitted in the discussion in Section 4. The explicit formula for the bulk band functions of $H_B(\mathbf{k})$ is

$$E_{\pm}(\mathbf{k}) = f(\mathbf{k}) \pm \sqrt{g_1(\mathbf{k}) + g_2(\mathbf{k})}, \quad (\text{C.1})$$

where

$$\begin{aligned} f(\mathbf{k}) &:= 2t' \cos(\phi) [\cos(k_1) + \cos(k_2) + \cos(k_1 - k_2)] \\ g_1(\mathbf{k}) &:= |t|^2 (|1 + \cos(k_1) + \cos(k_2)|^2 + |\sin(k_1) + \sin(k_2)|^2) \\ g_2(\mathbf{k}) &:= |V + 2t' \sin(\phi)(\sin(k_1) - \sin(k_2) - \sin(k_1 - k_2))|^2. \end{aligned} \quad (\text{C.2})$$

The explicit action of the Bloch-reduced edge Hamiltonian $H_E(k)$ in $\ell^2(\mathbb{N}; \mathbb{C}^2)$ is

$$\begin{aligned} \left(\hat{H}_E(k) \tilde{\psi}(k) \right)_m &:= \\ t \left(\begin{pmatrix} (1 + e^{-ik_2}) \tilde{\psi}_m^B(k) + \tilde{\psi}_{m-1}^B(k) \\ (1 + e^{ik_2}) \tilde{\psi}_m^A(k) + \tilde{\psi}_{m+1}^A(k) \end{pmatrix} + V \begin{pmatrix} \tilde{\psi}_m^A(k) \\ -\tilde{\psi}_m^B(k) \end{pmatrix} \right) &+ \\ + t' \left(\begin{pmatrix} e^{i\phi} \left(e^{ik_2} \tilde{\psi}_m^A(k) + \tilde{\psi}_{m-1}^A(k) + e^{-ik_2} \tilde{\psi}_{m+1}^A(k) \right) + e^{-i\phi} \left(e^{-ik_2} \tilde{\psi}_m^A(k) + \tilde{\psi}_{m+1}^A(k) + e^{ik_2} \tilde{\psi}_{m-1}^A(k) \right) \\ e^{i\phi} \left(e^{-ik_2} \tilde{\psi}_m^B(k) + \tilde{\psi}_{m+1}^B(k) + e^{ik_2} \tilde{\psi}_{m-1}^B(k) \right) + e^{-i\phi} \left(e^{ik_2} \tilde{\psi}_m^B(k) + \tilde{\psi}_{m-1}^B(k) + e^{-ik_2} \tilde{\psi}_{m+1}^B(k) \right) \end{pmatrix} \right), & \end{aligned} \quad (\text{C.3})$$

subject to the boundary condition $\psi_{-1}(k) = 0$.

Acknowledgements

This work was supported by a Research Fellowship at Trinity College Cambridge (MJC), a Fondation Sciences Mathématiques de Paris Postdoctoral Fellowship at École Normale Supérieure (MJC), ARO MURI Award No. W911NF-14-0247 (ABW), and NSF DMREF Award No. 1922165 (ABW). The authors are grateful to Jacob Shapiro for helpful discussions.

References

- [1] N. Ashcroft and N. Mermin. *Solid State Physics*. Saunders College, 1976.
- [2] J. E. Avron, R. Seiler, and B. Simon. Charge deficiency, charge transport and comparison of dimensions. *Communications in Mathematical Physics*, 159(2):399–422, 1994.
- [3] G. Bal, S. Becker, A. Drouot, C. F. Kammerer, J. Lu, and A. Watson. Edge state dynamics along curved interfaces, 2021. [arXiv:2106.00729](#).
- [4] A. Bastounis, A. C. Hansen, and V. Vlačić. The extended Smale’s 9th problem - on computational barriers and paradoxes in estimation, regularisation, learning and computer-assisted proofs. *Preprint*, 2021.
- [5] S. Becker and A. Hansen. Computing solutions of Schrödinger equations on unbounded domains - On the brink of numerical algorithms. 2020. [arXiv:2010.16347](#).
- [6] J. Bellissard, A. Van Elst, and H. Schulz-Baldes. The noncommutative geometry of the quantum Hall effect. *Journal of Mathematical Physics*, 35(10):5373–5451, 1994.
- [7] J. Ben-Artzi, M. J. Colbrook, A. C. Hansen, O. Nevanlinna, and M. Seidel. Computing spectra - On the solvability complexity index hierarchy and towers of algorithms. 2020. [arXiv:1508.03280](#).
- [8] J. Ben-Artzi, M. Marletta, and F. Rösler. Computing scattering resonances. 2020. [arXiv:2006.03368](#).
- [9] J. Ben-Artzi, M. Marletta, and F. Rösler. Computing the sound of the sea in a seashell. *Foundations of Computational Mathematics*, pages 1–35, 2021.
- [10] J. Ben-Artzi, M. Marletta, and F. Rösler. Universal algorithms for computing spectra of periodic operators. 2021. [arXiv:2104.09575](#).
- [11] B. A. Bernevig and T. L. Hughes. *Topological Insulators and Topological Superconductors*. Princeton University Press, 2013.
- [12] M. V. Berry. Quantal phase factors accompanying adiabatic changes. In *Proceedings of the Royal Society of London A: Mathematical, Physical and Engineering Sciences*, volume 392, pages 45–57. The Royal Society, 1984.
- [13] A. J. Bestwick, E. J. Fox, X. Kou, L. Pan, K. L. Wang, and D. Goldhaber-Gordon. Precise quantization of the anomalous Hall effect near zero magnetic field. *Physical Review Letters*, 114(18):1–5, 2015.
- [14] P. Billingsley. *Convergence of Probability Measures*. John Wiley & Sons, second edition, 1999.
- [15] L. Blum, F. Cucker, M. Shub, and S. Smale. *Complexity and Real Computation*. Springer-Verlag New York, Inc., 1998.
- [16] L. Blum, M. Shub, and S. Smale. On a theory of computation and complexity over the real numbers: NP-completeness, recursive functions and universal machines. *American Mathematical Society. Bulletin.*, 21(1):1–46, 1989.
- [17] A. Bols and A. H. Werner. Absolutely Continuous Edge Spectrum of Hall Insulators on the Lattice. *Annales Henri Poincaré*, 2021.
- [18] J. Braun and C. Ortner. Sharp Uniform Convergence Rate of the Supercell Approximation of a Crystalline Defect. *SIAM Journal on Numerical Analysis*, 58(1):279–297, 2020.
- [19] C. Buchendorfer and G. M. Graf. Scattering of magnetic edge states. *Annales Henri Poincaré*, 7(2):303–333, 2006.
- [20] C. Z. Chang et. al. Experimental observation of the quantum anomalous Hall effect in a magnetic topological Insulator. *Science*, 340(6129):167–170, 2013.
- [21] C. Z. Chang et. al. High-precision realization of robust quantum anomalous Hall state in a hard ferromagnetic topological insulator. *Nature Materials*, 14(5):473–477, 2015.
- [22] M. J. Colbrook. On the computation of geometric features of spectra of linear operators on Hilbert spaces. 2019.
- [23] M. J. Colbrook. *The Foundations of Infinite-Dimensional Spectral Computations*. PhD thesis, University of Cambridge, 2020.
- [24] M. J. Colbrook. Pseudoergodic operators and periodic boundary conditions. *Mathematics of Computation*, 89(322):737–766, 2020.
- [25] M. J. Colbrook. Computing spectral measures and spectral types. *Communications in Mathematical Physics*, 384(1):433–501, 2021.
- [26] M. J. Colbrook. Unscrambling the infinite: Can we compute spectra? *IMA Mathematics Today*, 2021. URL: <https://ima.org.uk/16912/unscrambling-the-infinite-can-we-compute-spectra/>.

- [27] M. J. Colbrook. Computing semigroups with error control. *SIAM Journal on Numerical Analysis*, to appear.
- [28] M. J. Colbrook, V. Antun, and A. C. Hansen. Can stable and accurate neural networks be computed? - On the barriers of deep learning and Smale's 18th problem. *Proceedings of the National Academy of Sciences*, to appear.
- [29] M. J. Colbrook and L. Ayton. A contour method for time-fractional PDEs and an application to fractional viscoelastic beam equations. 2021. [arXiv:2111.13070](https://arxiv.org/abs/2111.13070).
- [30] M. J. Colbrook and A. C. Hansen. On the infinite-dimensional QR algorithm. *Numerische Mathematik*, 143(1):17–83, 2019.
- [31] M. J. Colbrook and A. C. Hansen. The foundations of spectral computations via the solvability complexity index hierarchy. 2020. [arXiv:1908.09592](https://arxiv.org/abs/1908.09592).
- [32] M. J. Colbrook and A. Horning. SpecSolve, 2020. URL: <https://github.com/SpecSolve/SpecSolve>.
- [33] M. J. Colbrook, A. Horning, K. Thicke, and A. B. Watson. SpecTB, 2021. URL: <https://github.com/SpecSolve/SpecTB>.
- [34] M. J. Colbrook, A. Horning, and A. Townsend. Computing spectral measures of self-adjoint operators. *SIAM Review*, 63(3):489–524, 2021.
- [35] M. J. Colbrook, B. Roman, and A. C. Hansen. How to compute spectra with error control. *Phys. Rev. Lett.*, 122:250201, 2019.
- [36] J. M. Combes and L. Thomas. Asymptotic behaviour of eigenfunctions for multiparticle Schrödinger operators. *Communications in Mathematical Physics*, 34(4):251–270, 1973.
- [37] E. B. Davies and M. Plum. Spectral pollution. *IMA Journal of Numerical Analysis*, 24(3):417–438, 2004.
- [38] P. Delplace, J. B. Marston, and A. Venaille. Topological origin of equatorial waves. *Science*, 358(6366):1075–1077, 2017.
- [39] B. Dingfelder and J. A. C. Weideman. An improved Talbot method for numerical Laplace transform inversion. *Numer. Algorithms*, 68(1):167–183, 2015.
- [40] P. Doyle and C. McMullen. Solving the quintic by iteration. *Acta Math.*, 163(3-4):151–180, 1989.
- [41] A. Drouot. Microlocal Analysis of the Bulk-Edge Correspondence. *Communications in Mathematical Physics*, 383(3):2069–2112, 2021.
- [42] V. Ehrlicher, C. Ortner, and A. V. Shapeev. Analysis of Boundary Conditions for Crystal Defect Atomistic Simulations. *Archive for Rational Mechanics and Analysis*, 222(3):1217–1268, 2016.
- [43] A. Elgart, G. M. Graf, and J. H. Schenker. Equality of the bulk and edge Hall conductances in a mobility gap. *Communications in Mathematical Physics*, 259(1):185–221, 2005.
- [44] C. Fefferman and L. Seco. On the energy of a large atom. *Bull. Amer. Math. Soc. (N.S.)*, 23(2):525–530, 1990.
- [45] C. Fefferman and L. Seco. Interval arithmetic in quantum mechanics. In *Applications of interval computations (El Paso, TX, 1995)*, volume 3 of *Appl. Optim.*, pages 145–167. Kluwer Acad. Publ., Dordrecht, 1996.
- [46] J. Fröhlich, G. M. Graf, and J. Walcher. On the extended nature of edge states of Quantum Hall Hamiltonians. *Annales Henri Poincaré*, 1(3):405–442, 2000.
- [47] M. Fruchart and D. Carpentier. An introduction to topological insulators. *Comptes Rendus Physique*, 14(9):779–815, 2013.
- [48] I. Gavriluk, V. Makarov, and V. Vasylyk. *Exponentially convergent algorithms for abstract differential equations*. Springer Science & Business Media, 2011.
- [49] I. Gavriluk and V. L. Makarov. Exponentially convergent parallel discretization methods for the first order evolution equations. *Comput. Methods Appl. Math.*, 1(4):333–355, 2001.
- [50] François Germinet, Abel Klein, and Jeffrey H. Schenker. Dynamical delocalization in random Landau Hamiltonians. *Annals of Mathematics*, 166(1):215–244, 2007.
- [51] M. J. Gilbert. Topological electronics. *Communications Physics*, 4(1):1–12, 2021.
- [52] M. A. Gilles and A. Townsend. Continuous analogues of Krylov subspace methods for differential operators. *SIAM J. Numer. Anal.*, 57(2):899–924, 2019.
- [53] G. M. Graf and M. Porta. Bulk-edge correspondence for two-dimensional topological insulators. *Communications in Mathematical Physics*, 324(3):851–895, 2013.
- [54] G. M. Graf and J. Shapiro. The Bulk-Edge Correspondence for Disordered Chiral Chains. *Communications in Mathematical Physics*, 363(3):829–846, 2018.

- [55] F. D. M. Haldane. Model for a Quantum Hall Effect without Landau Levels: Condensed-Matter Realization of the "Parity Anomaly". *Physical Review Letters*, 61(18):2015–2018, 1988.
- [56] N. Hale and L. N. Trefethen. New quadrature formulas from conformal maps. *SIAM J. Num. Anal.*, 46(2):930–948, 2008.
- [57] T. Hales. A proof of the Kepler conjecture. *Annals of Mathematics (2)*, 162(3):1065–1185, 2005.
- [58] T. Hales et al. A formal proof of the Kepler conjecture. *Forum Math. Pi*, 5:e2, 29, 2017.
- [59] B. I. Halperin. Quantized Hall conductance, current-carrying edge states, and the existence of extended states in a two-dimensional disordered potential. *Phys. Rev. B*, 25(4):2185–2190, 1982.
- [60] A. C. Hansen. On the solvability complexity index, the n -pseudospectrum and approximations of spectra of operators. *Journal of the American Mathematical Society*, 24(1):81–124, 2011.
- [61] M. Z. Hasan and C. L. Kane. Colloquium: Topological Insulators. *Rev. Mod. Phys.*, 82(4):3045–3067, 2010.
- [62] Y. Hatsugai. Chern number and edge states in the integer quantum Hall effect. *Phys. Rev. Lett.*, 71(22):3697–3700, 1993.
- [63] P. D. Hislop and I. M. Sigal. *Introduction to Spectral Theory*, volume 113. Springer-Verlag New York, 1996.
- [64] A. Horning and A. Townsend. FEAST for differential eigenvalue problems. *SIAM J. Numer. Anal.*, 58(2):1239–1262, 2020.
- [65] D. Johnstone, M. J. Colbrook, A. E. B. Nielsen, P. Öhberg, and C. W. Duncan. Bulk localised transport states in infinite and finite quasicrystals via magnetic aperiodicity. 2021. [arXiv:2107.05635](#).
- [66] J. Kellendonk, T. Richter, and H. Schulz-Baldes. Edge current channels and Chern numbers in the integer quantum Hall effect. *Reviews in Mathematical Physics*, 14(01):87–119, 2002.
- [67] J. Kellendonk and H. Schulz-Baldes. Boundary maps for C^* -crossed products with an application to the quantum Hall effect. *Communications in Mathematical Physics*, 249(3):611–637, 2004.
- [68] J. Kellendonk and H. Schulz-Baldes. Quantization of edge currents for continuous magnetic operators. *Journal of Functional Analysis*, 209(2):388–413, 2004.
- [69] A. Kitaev. Periodic table for topological insulators and superconductors. *AIP Conference Proceedings*, 1134(1):22–30, 2009.
- [70] P. Kuchment. An overview of periodic elliptic operators. *Bulletin of the American Mathematical Society*, 53(3):343–414, 2016.
- [71] J. P. Lee-Thorp. *Bifurcation perspective on topologically protected and non-protected states in continuous systems*. PhD thesis, Columbia University, 2016.
- [72] J. P. Lee-Thorp, M. I. Weinstein, and Y. Zhu. Elliptic operators with honeycomb symmetry: Dirac points, edge states and applications to photonic graphene. *Archive for Rational Mechanics and Analysis*, 232(1):1–63, 2019.
- [73] M. Lewin and É. Séré. Spectral pollution and how to avoid it. *Proceedings of the London Mathematical Society*, 100(3):864–900, 2010.
- [74] M. López-Fernández, C. Palencia, and A. Schädle. A spectral order method for inverting sectorial Laplace transforms. *SIAM J. Numer. Anal.*, 44(3):1332–1350, 2006.
- [75] M. Ludewig and G. C. Thiang. Cobordism invariance of topological edge-following states. 2:1–38, 2020. [arXiv:2001.08339](#).
- [76] G. Marcelli, D. Monaco, M. Moscolari, and G. Panati. The Haldane model and its localization dichotomy, 2019. [arXiv:1909.03298](#).
- [77] W. McLean and V. Thomée. Time discretization of an evolution equation via Laplace transforms. *IMA J. Appl. Math.*, 24(3):439–463, 2004.
- [78] C. McMullen. Families of rational maps and iterative root-finding algorithms. *Annals of Mathematics (2)*, 125(3):467–493, 1987.
- [79] C. McMullen. Braiding of the attractor and the failure of iterative algorithms. *Invent. Math.*, 91(2):259–272, 1988.
- [80] J. Michala, A. Pierson, T. Loring, and A. Watson. Wave-packet propagation in a finite topological insulator and the spectral localizer index. *Involve*, 14(2):209–239, 2021.
- [81] J. E. Moore. The birth of topological insulators. *Nature*, 464(7286):194–198, 2010.
- [82] M. Nakahara. *Geometry, topology and physics*. CRC press, 2018.

- [83] A. Pokrzywa. Method of orthogonal projections and approximation of the spectrum of a bounded operator. *Studia Mathematica*, 65(1):21–29, 1979.
- [84] E. Prodan and H. Schulz-Baldes. *Bulk and Boundary Invariants for Complex Topological Insulators*. Mathematical Physics Studies. Springer International Publishing, 2016.
- [85] X. L. Qi and S. C. Zhang. Topological insulators and superconductors. *Reviews of Modern Physics*, 83(4), 2011.
- [86] M. C. Rechtsman, J. M. Zeuner, Y. Plotnik, Y. Lumer, D. Podolsky, F. Dreisow, S. Nolte, M. Segev, and A. Szameit. Photonic Floquet topological insulators. *Nature*, 496(7444):196–200, 2013.
- [87] M. Reed and B. Simon. *Methods of Modern Mathematical Physics, IV: Analysis of Operators*. Academic press, 1977.
- [88] M. Reed and B. Simon. *Methods of Modern Mathematical Physics. I*. Academic Press, Inc., Harcourt Brace Jovanovich, New York, second edition, 1980.
- [89] A. W. Rodriguez, A. P. McCauley, Y. Avniel, and S. G. Johnson. Computation and visualization of photonic quasicrystal spectra via Bloch’s theorem. *Phys. Rev. B*, 77(10):104201, 2008.
- [90] F. Rösler and A. Stepanenko. Computing eigenvalues of the Laplacian on rough domains. 2021. [arXiv:2104.09444](#).
- [91] A. P. Schnyder, S. Ryu, A. Furusaki, and A. Ludwig. Classification of Topological Insulators and Superconductors. *AIP Conference Proceedings*, 1134(1):10–21, 2009.
- [92] H. Schulz-Baldes and J. Bellissard. A kinetic theory for quantum transport in aperiodic media. *Journal of Statistical Physics*, 91(5-6):991–1026, 1998.
- [93] H. Schulz-Baldes, J. Kellendonk, and T. Richter. Simultaneous quantization of edge and bulk Hall conductivity. *Journal of Physics A: Mathematical and Theoretical*, 33(2):L27—L32, 1999.
- [94] D. Sheen, I. H. Sloan, and V. Thomée. A parallel method for time discretization of parabolic equations based on Laplace transformation and quadrature. *IMA J. Numer. Anal.*, 23(2):269–299, 2003.
- [95] S. Smale. The fundamental theorem of algebra and complexity theory. *American Mathematical Society. Bulletin.*, 4(1):1–36, 1981.
- [96] S. Smale. Complexity theory and numerical analysis. *Acta Numer.*, 6:523–551, 1997.
- [97] S. Soussi. Convergence of the Supercell Method for Defect Modes Calculations in Photonic Crystals. *SIAM Journal on Numerical Analysis*, 43(3):1127–1175, 2005.
- [98] E. M. Stein and R. Shakarchi. *Real Analysis: Measure Theory, Integration, and Hilbert Spaces*. Princeton University Press, 2009.
- [99] R. Süssstrunk and S. D. Huber. Observation of phononic helical edge states in a mechanical topological insulator. *Science*, 349(6243):47–50, 2015.
- [100] C. Tauber and G. C. Thiang. Topology in shallow-water waves: A spectral flow perspective. pages 1–19, 2021. [arXiv:2110.04097](#).
- [101] K. Thicke, A. B. Watson, and J. Lu. Computing Edge States without Hard Truncation. *SIAM Journal on Scientific Computing*, 43(2):B323–B353, 2021.
- [102] D. J. Thouless, M. Kohmoto, M. P. Nightingale, and M. den Nijs. Quantized Hall Conductance in a Two-Dimensional Periodic Potential. *Phys. Rev. Lett.*, 49(6):405–408, 1982.
- [103] L. N. Trefethen and J. A. C. Weideman. The exponentially convergent trapezoidal rule. *SIAM Rev.*, 56(3):385–458, 2014.
- [104] D. Vanderbilt. *Berry Phases in Electronic Structure Theory: Electric Polarization, Orbital Magnetization and Topological Insulators*. Cambridge University Press, 2018.
- [105] Z. Wang, Y. Chong, J. D. Joannopoulos, and M. Soljacic. Observation of unidirectional backscattering-immune topological electromagnetic states. *Nature*, 461:772–775, 2009.
- [106] M. Webb. *Isospectral algorithms, Toeplitz matrices and orthogonal polynomials*. PhD thesis, University of Cambridge, 2017.
- [107] M. Webb and S. Olver. Spectra of Jacobi operators via connection coefficient matrices. *Communications in Mathematical Physics*, 382(2):657–707, 2021.
- [108] J. A. C. Weideman. Improved contour integral methods for parabolic PDEs. *IMA J. Numer. Anal.*, 30(1):334–350, 2010.
- [109] J. A. C. Weideman and L. N. Trefethen. Parabolic and hyperbolic contours for computing the Bromwich integral. *Math. Comp.*, 76(259):1341–1356, 2007.